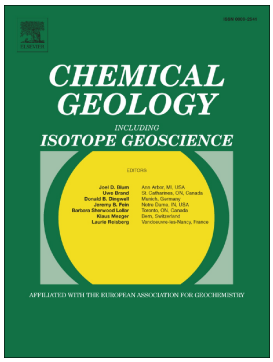

A deep fluid source of radiogenic Sr and highly dynamic seepage conditions recorded in Miocene seep carbonates of the northern Apennines (Italy)

C. Argentino, F. Lugli, A. Cipriani, S. Conti, D. Fontana

PII: S0009-2541(19)30261-X
DOI: https://doi.org/10.1016/j.chemgeo.2019.05.029
Reference: CHEMGE 19188

To appear in: *Chemical Geology*

Received date: 20 December 2018
Revised date: 17 May 2019
Accepted date: 18 May 2019

Please cite this article as: C. Argentino, F. Lugli, A. Cipriani, et al., A deep fluid source of radiogenic Sr and highly dynamic seepage conditions recorded in Miocene seep carbonates of the northern Apennines (Italy), Chemical Geology, https://doi.org/10.1016/j.chemgeo.2019.05.029

A deep fluid source of radiogenic Sr and highly dynamic seepage conditions recorded in Miocene seep carbonates of the northern Apennines (Italy).

Argentino C.[a,b*], Lugli F. [a,c], Cipriani A. [a,d*], Conti S. [a], Fontana D.[a]

[a] Department of Chemical and Geological Sciences, University of Modena and Reggio Emilia, 41125 Modena, Italy.
[b] Centre for Arctic Gas Hydrate, Environment and Climate, The Arctic University of Norway (UiT), 9037 Tromsø, Norway.
[c] Department of Cultural Heritage, University of Bologna, 40126 Bologna, Italy.
[d] Lamont-Doherty Earth Observatory of Columbia University, Palisades, 10964 New York, USA.
*Corresponding authors: claudio.argentino@unimore.it; anna.cipriani@unimore.it

Abstract

The $^{87}Sr/^{86}Sr$, REE and Mo-U systematics were investigated in Miocene seep carbonates formed on accretionary ridges at the front of the northern Apennine wedge. Here we evaluate fluid sources, seepage intensity and redox conditions during carbonate precipitation. Micrite matrix and early calcite cements lining cavities are the main authigenic carbonate phases and show negligible diagenetic alteration. Their AOM-related (anaerobic oxidation of methane) origin is evident from $\delta^{13}C$ values ranging from -38.7‰ to -25.7‰. The $^{87}Sr/^{86}Sr$ ratios in carbonates vary between 0.708659 and 0.709132. Most micrite values fall within the range of Middle Miocene seawater (Langhian, MNN5a biozone), in agreement with the biostratigraphy of the host sediments, thus reflecting precipitation of seep carbonates close to the seafloor. Highly radiogenic $^{87}Sr/^{86}Sr$ ratios, of early calcite cements and micrite from conduit-rich facies at the base of carbonate bodies, likely derived from the interaction of fluids with detrital clays during the fault-controlled upward migration through the underlying terrigenous turbidite successions. Strong Mo and U enrichments in carbonates, with Mo_{EF} and U_{EF} up to 233.5 and 86.6 respectively, coupled with $(Mo/U)_{EF}$ ratios ranging between 0.7 and 9.7, indicate dynamic redox conditions, episodically sulfidic and restricted to porewaters. This interpretation is also supported by enrichments in MREE of micrites and a general absence of negative Ce anomalies. These new data provide an indirect indication of rates and temporal variability of AOM at fossil methane seeps developed on a thrust related anticline and help to constrain the complex interaction

between fluid migration pathways, seepage intensity and environmental conditions as observed in modern seep analogues.

Key words
Seep carbonates, $^{87}Sr/^{86}Sr$, REE, fluid source, molybdenum enrichment, seepage dynamics.

1. Introduction

Marine seepage accounts today for ~20 Tg per year of methane emissions (Anderson et al., 2012). An evaluation of its contribution to global greenhouse gas emissions requires a deep understanding of the process of anaerobic oxidation of methane, and its spatial and temporal variability (AOM, Boetius et al., 2000). Our knowledge of cold seeps has greatly benefited from the study of methane-derived carbonates from the fossil record, which reflect the long-term evolution of seepage systems in space and time (e.g. Campbell, 2006; Conti et al., 2010, 2017; Feng et al., 2009a, b; Jakubowicz et al., 2015; Malone et al., 2012). Geochemical data on seep carbonates informs on fluid expulsion processes, composition of precipitating fluids, seepage intensity and rates of AOM (e.g. Aloisi et al., 2000; Greinert et al., 2001; Malone et al., 2012; Naehr et al., 2007; Peckmann et al., 2001; Roberts, 2001). Moreover, the application of Strontium Isotope Stratigraphy (SIS, McArthur et al., 2001) to authigenic carbonates has proved to be a successful tool to obtain reliable formation ages (Ge and Jiang, 2013; Kiel et al., 2014; Kiel and Hansen, 2015). In fact, the $^{87}Sr/^{86}Sr$ isotope composition of seep carbonates reflects the Sr signature of the precipitating fluids (Burke et al., 1982; Joseph et al., 2012; Solomon et al., 2009; Teichert et al., 2005; Torres et al., 2004; Veizer, 1989) and seep carbonates forming close to the seafloor generally show $^{87}Sr/^{86}Sr$ values of coeval seawater (Naehr et al., 2000). Deviation from the expected Sr isotope ratios in weakly altered carbonates possibly indicates mixing with fluids modified by fluid/rock interaction processes (Hong et al., 2018; Joseph et al., 2012; Sample et al., 1993; Tong et al., 2013; Viola et al., 2017). Such a complex situation is common at accretionary wedges. In these settings, carbonates precipitate from a mix of seawater and deeper fluids, bringing hydrocarbons toward the seafloor through different migration pathways (Joseph et al. 2012; Teichert et al. 2005; Torres et al. 2004).

In authigenic carbonates, rare earth elements (REE) are commonly used to reconstruct interstitial redox conditions and to trace the evolution of early diagenetic fluids (e.g. Birgel et al.,

2011; Himmler et al., 2010; Hu et al., 2014; McRae et al., 1992, Wang et al., 2015; Zwicker et al., 2018). Carbonates forming under normal marine conditions in oxygenated waters follow the smooth seawater REE profile, characterized by enrichments in HREE along with positive La and negative Ce anomalies (Elderfield et al., 1990). Deviations from the seawater pattern may correspond to differential incorporation of redox sensitive elements (such as Ce, MREE) under suboxic or anoxic conditions, or be related to admixture with fluids contaminated by fluid-rock interaction processes (Bayon et al., 2011; Frimmel, 2010; Kim et al., 2012; Sarkar et al., 2003). In oxic pore-waters, Ce(III) is partially oxidized to Ce(IV) on the surface of Fe-Mn oxyhydroxides, leaving a typical negative Ce anomaly in fluids, which is eventually recorded by authigenic phases within the sediments (Frimmel, 2010; Shields and Webb, 2004). Conversely, positive Ce anomalies represent precipitation in anoxic to suboxic porewaters. Methane-derived carbonates are characterized by a wide range of Ce concentrations, with positive anomalies indicative of precipitation under strictly anoxic conditions and negative or absent anomalies ascribed to episodic oxic conditions and seawater influences (Feng et al., 2010; Hu et al., 2014; Wang et al., 2015).

The recent application of redox sensitive Mo and U to the study of sediments and authigenic carbonates has advanced the comprehension of seepage dynamics and identification of paleo-seeps within the sedimentary column (Chen et al., 2016; Hu et al., 2017). In oxygenated seawater, Mo is mainly present as molybdate anion (MoO_4^{-2}) at uniformly high concentrations (~105 nM; Collier, 1985). Molybdenum is relatively unreactive in oxic conditions and is removed by slow adsorption to Mn-Fe oxyhydroxides (Morford et al., 2009; Zheng et al., 2000). Dissolved Mo becomes highly reactive under anoxic-sulfidic conditions above a threshold value of ~100 μM $[H_2S]_{(aq)}$, which favors the conversion of molybdate into thiomolybdate ($MoO_xS^2_{(4-X)}$, X= 0 to 3) (Erickson and Helz, 2000; Helz et al., 1996; Zheng et al., 2000). Thiomolybdate is readily adsorbed onto humic substances and Fe-Mn oxyhydroxides or sequestered by sulfide minerals, thus generating Mo concentrations above detrital values of 1-2 mg/kg (Helz et al., 1996; Magyar et al., 1993; Tribovillard et al., 2004). Since hydrogen sulfide production within the Sulfate-Methane Transition Zone (SMTZ) mainly reflects methane oxidation (Boetius et al., 2000), Mo enrichments may help evaluate the rate of AOM (Hu et al., 2014).

Uranium concentration in carbonates provides further insights into porewater redox conditions. Under oxic conditions, dissolved U occurs as U(VI) forming uranyl and uranyl

carbonate ions and shows a conservative geochemical behavior (Algeo and Tribovillard, 2009; Cumberland et al., 2016; Russell et al., 1994). Sediment uptake of U starts in suboxic porewaters at the Fe(III)-Fe(II) transition, when the soluble U(VI) is reduced to insoluble U(IV). Due to the larger size of uranyl ion relative to Ca(II), its partition coefficient in carbonate is low. The incorporation of U into authigenic carbonate phases is favored by a much higher partition coefficient in suboxic and anoxic porewaters because the ionic radius of U(IV) is similar to that of Ca(II) (Sturchio et al., 1998). The degree of enrichment of Mo and U relative to the average continental crust (Taylor and McLennan, 1985) allows a better understanding of the variations in porewater conditions and AOM intensity through time (Algeo and Tribovillard, 2009; Hu et al., 2014). Since U enrichment occurs within the Fe reduction zone, $(Mo/U)_{EF}$< 3.1 (Mo/U of present-day seawatwer) is generally associated with suboxic to anoxic conditions. Sulfidic interstitial conditions promote Mo accumulation and progressively increase the $(Mo/U)_{EF}$ ratio of sediments up to $(Mo/U)_{EF}$>3.1 (Algeo and Tribovillard, 2009).

In this paper, we report the $^{87}Sr/^{86}Sr$ ratios, REE and Mo-U systematics of Miocene seep carbonates formed atop an intrabasinal high in the inner foredeep of the Italian northern Apennines (Argentino et al., 2019). Active seeps from thrust-related ancticlines have been the object of several studies due to their close association with shallow gas hydrates (e.g. Greinert et al., 2001; Teichert et al., 2005; Torres et al., 2004); however, fossil examples are still poorly reported in the literature (Campbell, 2006 and references therein) or the structural setting often lack sufficient constraints for an accurate comparison with modern counterparts. This study aims to identify the origin of fluids involved in authigenic carbonate formation at a Miocene seep, to assess the contribution from deeply-derived fluids and to reconstruct seepage dynamics. We also tested the Strontium Isotope Stratigraphy (SIS) methodology (McArthur et al., 2001) on seep-related micrites using nannofossil biostratigraphy of the host sediments to corroborate the results.

2. Geological setting

2.1 The northern Apennines

The northern Apennine chain is an orogenic NE-verging wedge, characterized by the stacking of several structural units of oceanic and continental origin (Fig. 1). The complex structure of the chain is the result of the convergence and collision between the European and Africa plates, with the interposition of Adria and Corsica-Sardinia microplates, from the Mesozoic to the present (Carminati and Doglioni, 2012). The convergence stage started at the end of the Early Cretaceous, caused by the progressive consumption of the Piedmont-Ligurian Ocean, a portion of the Tethys. The complete closure of the ocean during Middle-Late Eocene caused the rapid uplift and erosion of the Alpine orogenic wedge and the inception of the continental collision. During the early stage of the collision (late Oligocene), the internal oceanic units (Ligurian nappe), which were deformed and accreted during the eo-meso-Alpine phases, were thrusted over the adjacent thinned margin of the continental Adria microplate, represented by Subligurian units. From Miocene to Recent, the thrust system migrated towards the foreland, involving the Tuscan and Umbrian-Marchean units (Fig. 1) deposited on the Adria microplate. The collisional stage was marked by the flexuring of the foreland and the formation of foredeep basins, progressively migrating towards NE (Argnani and Ricci Lucchi, 2001; Tinterri and Magalhaes, 2011). Small basins developed on top of the migrating accretionary wedge, filled by Epiligurian units (Conti et al., 2016; Ricci Lucchi, 1986). Thrust-related anticlines, occurring as intrabasinal highs in the foredeep, formed from the Burdigalian to the Messinian during different migratory phases of the foreland system (Conti et al., 2010, 2017 and references therein). Sedimentation on top of the intrabasinal highs (Fig. 1C) was mainly represented by hemipelagites and diluted turbidites (drape mudstones) up to hundred meter thick fine-grained intervals. Large seep carbonate bodies are hosted within these pelitic intervals at the front of the orogenic wedge and testify for a link between the seepage distribution and tectonic activity (Argentino et al., 2019).

2.2 The Corella outcrop

The Corella outcrop is located in the Tuscan Apennines, ~25 km northeast of Florence ([43°56'59"N 11°34'59.8"E] Fig. 1A). Seep carbonates are enclosed in a pelitic interval striking NW-SE, parallel to the structural trends of the chain and in proximity of the thrusting of the Tuscan units over the Marnoso-arenacea Fm. This interval is ~12 km long and up to 200 m in

thickess (Conti et al., 2017). The outcrop consists of six large authigenic bodies distributed in two stratigraphic horizons (L1, L3, L5 in the lower, and L2, L4, L6 in the upper; Fig. 1B). Carbonate bodies show stratiform to lenticular morphologies, up to 250 m in width and maximum thickness of 35 m, and are mainly formed of authigenic micrite locally enclosing fine-grained siliciclastic components. The basal portion of the carbonate bodies is dominated by conduit-rich facies and breccias with millimetre-sized clasts. Chemosynthetic communities, represented by articulated lucinids and vesicomyids, have been observed during fieldwork (Argentino et al., 2019). Based on calcareous nannofossil biostratigraphy of the enclosing marls, this outcrop has been ascribed to the Langhian MNN5a subzone (Conti et al., 2017).

3. Methods

Twenty-one samples of authigenic carbonates were collected from the Corella outcrop (Fig. 1). Most of the specimens derive from the carbonate body L1, which is the best exposed and easy to access; other samples were collected from L2, L4 and L5 carbonate bodies (Fig.1B). We have identified three different carbonate components based on petrographic observations (Fig. 2A,B): 1) authigenic micrite, dark grey to brown in color, locally rich in pyrite and with dispersed fine siliciclastic grains (matrix micrite); 2) early calcite cement lining and filling cavities and fractures (rim cement), commonly formed by anhedral to subhedral cloudy crystals; 3) lucinid shell fragments. The center of cavities and veins are filled by large, generally limpid, blocky calcite crystals likely related to late diagenetic processes that have not been considered in this study (Fig. 2). Table 1 reports sample location and the different types of carbonate components.

Carbon and oxygen stable isotopes were analyzed in 10 specimens of matrix micrite and rim cement obtained from 5 samples. Powders were obtained from polished slabs using a handheld microdrill and about 10 mg were reacted with 100% phosphoric acid at 25 °C for 24 h. The purified CO_2 gas was analyzed using a Finnigan MAT Delta S stable isotope mass spectrometer at the Department of Chemical, Life and Environmental Sustainability of the University of Parma. Results are reported in standard δ notation relative to the Vienna-PeeDee Belemnite (V-PDB) standard. Precision is 0.1‰ (1σ) for both $\delta^{13}C$ and $\delta^{18}O$ values.

Trace element concentrations in micrite and rim cements were measured in situ on rock slabs at the Centro Interdipartimentale Grandi Strumenti (C.I.G.S.) of the University of Modena

e Reggio Emilia using a 213 nm Nd:YAG laser ablation system (New Wave Research) coupled to a quadrupole ICP-MS (Thermo Fisher Scientific X-SeriesII). Analyses were obtained by firing at 10 Hz an 80 μm diameter circular laser spot for 30 s. Ablations were conducted in a stream of He, at a constant flux of ~600 ml/min, with a laser energy of ~10 J/cm^2. Each ablation was preceded by a 100 μm-size pre-ablation step (dwelling-time: 5 s., 10 Hz laser fire) to remove possible surface contaminations. Data were acquired for ^{24}Mg, ^{31}P, ^{39}K, ^{44}Ca, ^{47}Ti, ^{51}V, ^{52}Cr, ^{55}Mn, ^{57}Fe, ^{65}Cu, ^{66}Zn, ^{75}As, ^{85}Rb, ^{88}Sr, ^{90}Zr, ^{96}Mo, ^{133}Cs, ^{137}Ba, ^{139}La, ^{140}Ce, ^{141}Pr, ^{146}Nd, ^{147}Sm, ^{153}Eu, ^{157}Gd, ^{159}Tb, ^{163}Dy, ^{165}Ho, ^{166}Er, ^{169}Tm, ^{172}Yb, ^{175}Lu, ^{202}Hg, ^{208}Pb, ^{232}Th, ^{238}U and data reduction was performed with the Plasma Lab® software (Thermo Scientific). During this analytical session, ThO^+/Th^+ has been maintained below 0.1%. The JCt-1 calcite standard (Okai et al., 2004) was analyzed as an unknown and its repeated measurements were used to check the analytical precision and accuracy. Average values of the selected masses in JCt-1 agree within the uncertainty of the recommended values (Okai et al., 2004). The ^{44}Ca concentration in each sample was determined by ICP-OES and used as an internal standard. We employed NIST 610, NIST 612 and NIST 614 (Jochum et al., 2011; Pearce et al., 1997) as external standards for instrumental drift correction and calibration purposes.

Rare earth elements composition of the micritic component was analyzed by solution ICP-MS, given that LA-ICP-MS analyses cannot avoid potential contamination from non-carbonate material due to the heterogeneous composition of micrite. About 50 mg of powdered sample obtained from the homogeneous micritic portions of the samples were rinsed with MilliQ in Teflon beakers and dried down on a hot plate. Residual powders were leached using 5% v/v acetic acid for ~24 h at room temperature to dissolve the carbonate component (Rongemaille et al., 2011). The obtained solutions were then centrifuged and the supernatant was transferred to new vials and evaporated at ~100 °C. Samples were finally diluted in 4% HNO_3 and analyzed using a Thermo Scientific XSeries 2 ICP-MS housed at the C.I.G.S. (University of Modena and Reggio Emilia). Replicate measurements (n=3) on each sample solution provided precision RSD better than 5%.

For Ca, Al, Sr and Mn determinations, 5 mg of powders were dissolved in 1 ml 16 N HNO_3 and 1 ml concentrated HF in Teflon beakers. The sealed beakers were left on a hot plate at 90 °C for ~24 h. Solutions were then dried and re-dissolved in 4% HNO_3. Analyses were performed on a Perkin-Elmer Optima 4200DV ICP-OES hosted at the Department of Chemical

and Geological Sciences, University of Modena and Reggio Emilia. Precision RSD (n=3) was better than 5% for Ca and better than 2% for Al, Sr and Mn.

For Sr isotope analysis, about 10 mg of powder was obtained by microdrilling polished surfaces of the rock slabs, subsequently rinsed three times with MilliQ water. After drying, each sample was leached two times using a solution of 0.3% w/w acetic acid to sequentially dissolve about 30% and 40% of the powdered material, following the procedure described in Li et al. (2011) and Vescogni et al. (2014). Solutions were then dried down and dissolved in 3 M HNO_3. Sr was separated from the matrix by ion exchange chromatography following procedures reported in Argentino et al. (2017a) and Weber et al. (2018). The whole procedure was conducted in a clean laboratory under a laminar flow hood, with a typical Sr blank <100 pg. Strontium isotope ratios were measured by the MC-ICP-MS (Thermo Scientific Neptune) housed at the CIGS (University of Modena and Reggio Emilia). Solutions were diluted to ~50 ppb and introduced into the Neptune using a desolvating system (ESI-APEX IR) and a 100 µl/min nebulizer. Samples and standards were analyzed in a static multicollection mode in a single block of 100 cycles with an integration time of 8.4 s per cycle. Mass bias normalization was performed using the exponential law and a $^{87}Sr/^{86}Sr$ ratio of 8.37520. Isobaric interferences of ^{86}Kr and ^{87}Rb on ^{86}Sr and ^{87}Sr species were corrected. The $^{87}Sr/^{86}Sr$ ratio was corrected for instrumental bias to a NBS-987 value of 0.710248 (Thirlwall, 1991). Repeated measurements of the NBS-987 standard during two analytical sessions yielded a mean $^{87}Sr/^{86}Sr$ value of 0.710233 ± 0.000014 and 0.710228 ± 0.000012 (2σ, n=19 in both sessions). $^{87}Sr/^{86}Sr$ ratios were converted into numerical ages using the regression curves LOWESS look-up Table version 5 (McArthur et al., 2012). Maximum and minimum ages were obtained respectively subtracting and adding the cumulative error (reported in parenthesis) to the mean isotopic value.

In this paper, we calculated REE anomalies as follow: $Ce/Ce^* = 3Ce_N /(2La_N + Nd_N)$, $Eu/Eu^* = 2Eu_N / (Sm_N + Gd_N)$, $Pr/Pr^* = 2PrN / (Ce_N + Nd_N)$ and $La/La^*=La_N/(3Pr_N -2Nd_N)$ where N refers to concentration normalized to the Post Archean Australian Shale (PAAS; Taylor and McLennan, 1985). Enrichment factors for Mo, U and As (respectively Mo_{EF}, U_{EF} and As_{EF}) were defined as follows: $X_{EF} = [(X / Al)$ sample $/(X / Al)$ reference], where X and Al are the weight concentrations of elements X and Al, respectively (Tribovillard et al., 2006). $X_{EF}>3$ represents a detectable authigenic enrichment whereas $X_{EF}>10$ is indicative of a moderate to strong enrichment (Algeo and Tribovillard, 2009).

4. Results

4.1 Stable C and O isotopes

The stable carbon and oxygen isotopes composition of the methane-derived carbonates (matrix micrite and rim cement) is presented in Tab. 2. The $\delta^{13}C$ values in the micritic component range from -26.6‰ to -34.1‰ (mean = −29.5‰, sd = 3.2‰, n = 5) whereas the $\delta^{18}O$ composition ranges from -2.9 to -0.3 (mean = −1.9‰, sd = 1.3‰, n = 5). Rim cements show $\delta^{13}C$ values comprised between -25.7‰ and -38.7‰ (mean = −30.2‰, sd = 5‰, n = 5) and $\delta^{18}O$ between -0.16‰ and -8.0‰ (mean = −4.6‰, sd = 3.1‰, n = 5). All samples show depleted $\delta^{13}C$ signatures indicative of incorporation of AOM-derived carbon.

4.2 *Sr isotopes*

The $^{87}Sr/^{86}Sr$ ratios in micrite from the carbonate body L1 range from 0.708659 to 0.709132 (Fig. 3). Fifteen $^{87}Sr/^{86}Sr$ values from L1 are concentrated in a narrow range, with values comprised between 0.708713 and 0.708808 (Tab. 1), whereas one sample (3M) at the base of the body, is remarkably more radiogenic with $^{87}Sr/^{86}Sr$ ratio of 0.709132. Four micritic samples collected from the basal portion of the other carbonate bodies (L2, L4, L5) are characterized by more radiogenic Sr isotope ratios with values between 0.708837 and 0.708980. Rim cements in all examined bodies (L1, L2, L5) show isotopic ratios from 0.708761 to 0.709132, generally higher than micrite. A lucinid shell collected at the base of L2 gives a $^{87}Sr/^{86}Sr$ ratio of 0.708802 (Tab. 1). In general, the most radiogenic specimens (3V and 3M, L4, L2_VA and L2_VB) are from the conduit-rich facies in the basal portion of bodies.

4.3 Rare earth elements and trace elements

The total REE content in the examined micrites ranges from 8.6 to 17.2 mg/kg whereas rim cements show lower values comprised between 0.1 and 14.9 mg/kg (Tab. 3). The PAAS-normalized REE patterns in micritic samples are characterized by minor LREE depletion (mean

Pr_N/Yb_N=0.8, sd=0.1, n=20) and variable Middle REE (MREE) enrichment (0.8< Pr_N/Sm_N<0.9; 0.9<Sm_N/Yb_N<1.3) that generates a bulge mainly in correspondence of Eu, Gd, Tb and Dy (Fig. 6A). The same samples show highly variable Ce and La anomalies (0.6 < Ce/Ce*<1.2; 0.6<La/La*<2.0) (Fig. 6B) and are marked by positive Eu anomalies (1.1<Eu/Eu* < 1.8) (Tab. 3). Rim cements have a REE content from 0.1 and 14.9 mg/kg and show either a flat shale-normalized REE distribution or small MREE bulge (0.6< Pr_N/Sm_N<1.0; 0.4<Sm_N/Yb_N<3.0). Cerium anomalies range between 0.7 and 1 while La and Eu anomalies are comprised between 1.3 and 6.4, and between 1.1 and 2.6, respectively.

Manganese content in micrite and rim cements ranges between 44 and 191 mg/kg and 34 and 236 mg/kg, respectively. Strontium content is comprised between 242 and 1662 mg/kg in micrite, and between 382 and 2285 mg/kg in rim cements. Molybdenum content in micritic samples varies between 0.6 and 34.4 mg/kg (Tab. 4); all samples exhibit detectable to substantial Mo enrichments 4.4< Mo_{EF} <233.5 (Tab. 4; Fig.7). Uranium concentration ranges between 0.2 and 9.4 mg/kg, corresponding to enrichment factors 0.9< U_{EF} <88.6 (Tab. 4; Fig.7). Arsenic concentration varies from 0.2 to 4.4 mg/kg and enrichment factor As_{EF} from 1.5 to 35.0 (Tab. 4). $(Mo/U)_{EF}$ ratios show a broad range of values from 0.7 and 9.7. Eight samples show $(Mo/U)_{EF}$ below that of seawater (~3.1, Algeo and Tribovillard, 2009), two samples (19, L5) has $(Mo/U)_{EF}$ ≃ $(Mo/U)_{SW}$ and 11 samples have $(Mo/U)_{EF}$ >$(Mo/U)_{SW}$. The rim cements have Mo concentration from < 0.1 to 3.0 mg/kg and U from < 0.01 up to 1.4 mg/kg; Al concentrations below detection limits do not allow normalization of Mo and U contents and the calculation of respective enrichment factors.

5. Discussion

5.1 Assessment of diagenetic alteration

Ancient marine carbonates may retain the original $^{87}Sr/^{86}Sr$ composition when unaffected by diagenetic alteration. This is also true if they have interacted with fluids characterized by a similar isotopic signature during early diagenesis or with fluids with low Sr concentration (Denison et al 1994). Post-depositional processes within carbonates generally lead to a decrease in Sr, Na, Mg and increase in Mn, Fe and Zn, since the concentrations of these elements are

different in seawater and diagenetic fluids (Brand and Veizer, 1980). Manganese and Fe^{2+} show a similar behavior in solution and a comparable distribution coefficient in carbonates (D>1); they are more soluble in reducing fluids and substitute for Ca^{2+} in the carbonate lattice. Strontium tends to concentrate in interstitial fluids (D<1) (Tucker and Wright, 1990). Thus, ancient seep carbonates preserving the original Sr isotopic composition are commonly characterized by Mn content <300 mg/kg (Ge and Jiang, 2013; Kiel et al., 2014). In our study, Mn values are below this threshold (Tab. 1) and consistent with literature reference values for well-preserved seep carbonates (Joseph et al., 2013) and normal marine limestones (e.g. Brand and Veizer, 1980; Denison et al. 1994). Moreover, Mn and Sr do not correlate with each other (Fig. 4A) or with $^{87}Sr/^{86}Sr$ ratios. Only rim cements $^{87}Sr/^{86}Sr$ ratios show a positive correlation with Sr (R^2=0.87) (Fig. 4B). However, this behavior is opposed to what we would expect for meteoric alteration and may reflect the original mineralogy, namely higher Sr in calcite recrystallized from aragonite. Carbonates with $\delta^{18}O$ signature close to coeval seawater are more likely to have preserved the original isotopic signal (Kiel et al., 2014). Our micrite $\delta^{18}O$ composition ranges from -2.8 ‰ to 0.3 ‰, close to the Miocene seawater signature (Tab. 2) (Zachos et al., 2001). The oxygen isotope composition of rim cements is more depleted than the adjacent micrite, but their $\delta^{13}C$ is similar and their Mn and Sr concentrations suggest a limited diagenetic alteration. It is possible that other factors such as fluid temperature may have controlled the oxygen isotope signature of rim cements. Additional evidences for negligible diagenetic alteration are the poor correlation between $\delta^{18}O$ and $\delta^{13}C$ (R^2 = 0.28, Fig. 4C), and the absence of mixing lines of $\delta^{13}C$ and $\delta^{18}O$ with $^{87}Sr/^{86}Sr$ ratios (R^2 = 0.14 for $\delta^{13}C$, R^2 = 0.35 for $\delta^{18}O$, Fig. 4D). Based on these observations, we assume that our samples preserved the original Sr isotope composition.

5.2 Sr isotope dating and fluid source characterization

Most samples of micrite in this study have $^{87}Sr/^{86}Sr$ ratios corresponding to Langhian seawater Sr composition (MNN5a biozone) (Tab. 1; Fig. 5), in agreement with the biostratigraphic age of the host sediments (Conti et al., 2017). These data indicate that carbonate precipitation occurred in equilibrium with coeval seawater or shallow porewaters (Peckmann et al., 2001). A lucinid shell sample (L2G) age is in agreement with the micrite Sr isotope-age, which means it formed at shallow depth, close to the seafloor. These results indicate that

Strontium Isotope Stratigraphy can be successfully applied to the micritic component of ancient seep carbonates when scarcely altered and formed at shallow SMTZ, in equilibrium with coeval seawater. A further prerequisite is that micrite should be free of older detrital carbonate particles, which may contaminate the Sr isotope composition and lead to misleading interpretations. Sample 15M Sr isotope composition corresponds to a converted age of 16.9 Ma, which is older than the host sediments. Although the analysis was conducted on a rather homogeneous micritic sample, (assessed by petrographic observations), some contamination from fine-grained detrital carbonate particles may have contributed to the older age (Fig. 5).

Recently, rim cements of seep carbonates have been identified as the preferable SIS target given that they are very dense and less susceptible to interaction with late diagenetic fluids (Kiel et al., 2014). However, they are sometimes very thin and difficult to sample and contamination with adjacent material cannot be completely ruled out. Our data show that Sr analysis of the micritic component gives reliable results and may extend the field of applicability of SIS to seep carbonates. However, a detailed assessment of the diagenetic alteration is always recommended prior to isotopic analyses.

Early calcite cements lining cavities and fractures located in the basal portion of the bodies (Fig. 3), are characterized by more radiogenic $^{87}Sr/^{86}Sr$ ratios, which in some samples (3M, 3V, L2_VB, L4, 2VA, 2VB) are remarkably high, with values up to 0.709132. These radiogenic ratios cannot be explained in terms of absolute age, but they reflect deviation from coeval seawater and, therefore, the involvement of fluids of different origin. It is widely accepted that alteration of clay minerals, deriving from weathering of continental crust with high Rb/Sr ratios, progressively releases radiogenic Sr into interstitial waters, thus accounting for the precipitation of carbonate cements with high Sr isotope composition (Sample et al., 1993; Veizer et al., 1989). In our case study, the underlying thick terrigenous turbidites of the Marnoso arenacea Fm. and deeper pelitic units rich in clay minerals, might have contributed the radiogenic Sr. Some minor contributions from detrital micas might be also expected (e.g. Peckmann et al., 2001). Diagenetic fluids enriched with radiogenic Sr were then conveyed toward to the seafloor by a thrust-fault active during the Middle Miocene at the front of the Apenninic wedge (Fig. 1C). A similar interpretation has also been proposed for radiogenic $^{87}Sr/^{86}Sr$ values in carbonates from a vertical fault at the deformation front of the Oregon accretionary wedge (Sample et al., 1993) and for the Shenhu seep carbonates (continental slope,

South China Sea; Tong et al., 2013). It is worth mentioning that locally, during carbonate precipitation, the deep radiogenic Sr signal can be masked by mixing with seawater, as the amount of Sr in seawater is much higher than in the seeping fluid (Tran et al., 2014).

5.3 Rare Earth Elements

Diagenetic processes generally alter the carbonate REE composition producing a negative correlation between Ce/Ce* and Dy_N/Sm_N, and a positive correlation between Ce/Ce* and ∑REE (Shields and Stille, 2001). No strong correlations are evident in our samples, so we can assume that they retained the original REE budget (Fig. 8A) (Shields and Stille, 2001). Recently, Zwicker et al. (2018) have argued that during recrystallization of aragonite to calcite, REEs do not necessarily behave conservatively if early diagenesis is influenced by evolving porewater composition due to different biogeochemical processes, as in the case of cold seep environments. They define a diagenetic trend in terms of Pr/Yb ratio and Mg/Sr ratio. Our data fall outside this trend, having higher Pr/Yb ratios and more variable Mg/Sr ratio. In addition, the Mn and Fe contents are low. Therefore, the REE abundances of calcites have not been affected by later-stage porefluid diagenesis and reflect the original composition of early phases. This is also based on the assessment of diagenetic alteration discussed in section 5.1, and on the relationships between Ce/Ce* and Dy_N/Sm_N (Fig. 8A) and between Ce/Ce* and ∑REE (Fig. 8B).

Micrites display highly reproducible REE patterns with evident MREE enrichment (Fig. 6A). The MREE bulge commonly characterizes suboxic pore-waters of the Fe-reduction zone due to early diagenetic reduction of Fe-Mn-oxyhydroxides (Bayon et al., 2011; Haley et al., 2004; Himmler et al., 2013). Under intense fluxes of CH_4-rich fluids, the sulfate-methane transition zone moves closer to the sediment-water interface and the geochemical redox zonation is compressed, with the Fe-reduction zone partly overlapping the SO_4-reduction zone. Thus, authigenic carbonates precipitating at the shallow sulfate-methane transition zone may record a MREE enrichment and potentially preserve it in the geologic record (e.g. Birgel et al., 2011; Chen et al., 2005; Feng et al., 2009a; Ge et al., 2010; Himmler et al., 2010; Hu et al., 2014; Pierre et al., 2014; Wang et al., 2018; Wang et al., 2015). Rim cements show small MREE enrichments or flat REE patterns indicative of intermittent redox conditions (Feng et al., 2009a). The ∑REE of the micrites ranges between 8.6 and 17.2 mg/kg (Tab. 3), similarly to modern seep

carbonates from the Gulf of Mexico (Feng et al., 2009b; Hu et al., 2014), Congo deep-sea fan (Feng et al., 2010), South China Sea (Ge et al., 2010), Gulf of Cadiz (Wang et al., 2015) as well as some ancient seep carbonates (Feng et al., 2009a). Rim cements tend to have lower ΣREE, from 0.1 to 14.9 mg/kg, similar to values reported in Himmler et al., (2010) for microcrystalline and botryoidal aragonite. Variations in the ΣREE of seep carbonates are linked to variations in the carbonate precipitation rate and seepage intensity. Slow rates favor the incorporation of REE and lead to high ∑REE concentrations (Ge et al., 2010), similarly to authigenic apatite (Wright et al., 1987). Variability in the REE content of authigenic carbonates can also be related to mixing with seawater, given the low ∑REE of the latter (Himmler et al., 2010). It is therefore difficult to prove whether the broad range of ΣREE values reported in the present study is due to variable precipitation rates or variable seawater contributions to the fluid budget. Most of the micritic samples in this study show no Ce anomalies or, in few samples, real negative Ce anomalies (Fig. 6B). These data are indicative of precipitation under variable redox conditions as frequently observed in modern and ancient seep carbonates (Feng et al., 2009a; Jakubowicz et al., 2015; Wang et al., 2018; Wang et al., 2014). Negative Ce anomalies in seep carbonates may derive from episodic oxic conditions and seawater influx during carbonate precipitation (Feng et al., 2009a) or from organic matter complexation (preferential uptake of dissolved Ce^{4+} by organic compounds) (Himmler et al., 2010; Kim et al., 2012). Although we cannot entirely rule out the complexation effect, the Mo/U_{EF} ratio of sample L5 (2.8) is very close to the seawater ratio (3.1), and the first interpretation is more convincing. Most rim cements show positive Ce anomalies that can be interpreted to reflect precipitation under reducing conditions (Fig. 6B). Apparent Eu anomalies may result from analytical artefacts related to the interference of barium oxides forming during ICP-MS measurement (Dulski, 1994; Jarvis et al., 1989; Qi et al., 2005). However, we rule out this possibility because there is no correlation between Eu/Eu* and Ba/Sm in micrites (Fig. 8B). On the other hand, rim cements are more susceptible to this artifact due the low Sm concentrations and high Ba content and show a strong positive correlation (R^2= 0.9) (Fig. 8B). The positive Eu anomalies in micrites likely reflect mixing of reducing porewater (positive anomaly) with variable proportions of seawater (no Eu anomaly). An additional factor to be considered is the possible contribution of deep-sourced fluids that generally carry a Eu-enriched signal generated by Eu fractionation at elevated temperature (Kim et al., 2012). Based on the geological context and our Sr isotope data, it is reasonable to assume that deeper

radiogenic fluids may have also influenced the REE budget and contributed, in part, to the development of positive Eu anomalies in porewater.

5.4 Mo and U enrichments and covariation

The Mo and U contents in Corella samples are highly variable (Tab. 3) and frequently exceed the reported average values of the upper continental crust (~ 2.7 mg/kg for U, 3.7 for Mo; Taylor and McLennan, 1985) and modern marine sediments (1-5 mg/kg both for U and Mo; Morford et al., 2009). Our results are similar to those reported for modern methane-derived carbonates and seep-impacted sediments (Chen et al., 2016; Hu et al., 2017; Li et al., 2016; Liang et al., 2017). In micrite samples, Mo varies between 0.6 and 34.4 mg/kg, similarly to other published data from seep carbonates showing concentrations up to 12.4 mg/kg (Liang et al., 2017). Some of the carbonates display evident authigenic enrichments with Mo_{EF} up to 233.5. As far as we know, this is the highest published value for methane-derived carbonates, and is similar to the value of Mo_{EF} =273.0 encountered in sediment profiles from active seep areas in South China Sea (Chen et al., 2016). High Mo_{EF} values (>100), found in three of our carbonates (3M, 10 and 30) reflect an episode of intense sulfate-driven AOM and the establishment of sulfidic porewater conditions. Scott and Lyons (2012) reported two distinct Mo ranges, one for environments with hydrogen sulfide confined to pore waters and one with sulfidic bottom waters. In the first case, Mo is about 10 mg/kg and rarely exceeds 20 mg/kg. In case of persistent euxinic bottom waters, enrichments have a much wider range with concentrations consistently >60 mg/kg up to 100 mg/kg (Scott and Lyons, 2012). In our samples, Mo concentration rarely exceeds 20 mg/kg and the highest value obtained (34.4 mg/kg, sample 3M) is below the 60 mg/kg threshold (Tab. 3). We suggest that episodic sulfidic conditions were mainly restricted to pore-waters and did not steadily influence the bottom water.

Interestingly, arsenic shows some detectable enrichments (As_{EF}>3). Similar enrichments have been reported in seep carbonates collected above a mud volcano site in the Gulf of Mexico (Hu et al., 2014) and were interpreted as generated by an efficient particulate shuttle process (Algeo and Tribovillard, 2009; Crusius et al., 1996; Emerson and Huested, 1991; Magyar et al., 1993; Morford et al., 2005). In this process, methane-rich brines, episodically reaching the bottom waters, may induce Mn and Fe oxyhydroxides formation in the water column efficiently

scavenging Mo and As from the surrounding seawater (Tribovillard et al., 2013). This particulate eventually sinks to the seafloor, becoming progressively buried and reduced within the anoxic zone. Released elements then become available for incorporation into iron sulfides and authigenic carbonates (Hu et al., 2014; Tribovillard et al., 2013). Further evidences for the involvement of the particulate shuttle control process in trace metal scavenging has been reported for Pliocene seep carbonates in Taiwan (southern Western Foothills, Taiwan; Wang et al., 2019). These carbonates are characterized by enrichments in Mo, As, and Sb that correlate with excess iron. Interestingly, the same samples show high $(Mo/U)_{EF}$ ratios but $U_{EF}<2$. Based on field constraints, they suggest that these enrichments are related to iron shuttle processes with no influence of deep ascending fluids. In our study, As_{EF} values show a clear positive correlation with Mo_{EF} ($R^2= 0.67$; Fig. 8) but lack any trend with Fe/Al ($R^2< 0.1$; Fig. 8). We suggest that, rather than seawater, the source of As were the upward migrating fluids. The Corella seep carbonates thus represent an example of structurally controlled seepage system where trace metal enrichments are not influenced by the particulate shuttle process.

The U concentration in micrite samples varies between 0.2 and 9.4 mg/kg and is similar to values reported from modern seep carbonates, e.g. Liang et al., (2017) (2.0 up to 13.6 mg/kg) and Hu et al., 2014 (0.3 up to 8.6 mg/kg). Substantial authigenic enrichments ($U_{EF}>10$; Algeo and Tribovillard, 2009) up to 86.6 in our samples (Tab. 3; Fig. 6), are indicative of strictly anoxic redox conditions (Li et al., 2016).

Our data show a range of $(Mo/U)_{EF}$ between 0.7 and 9.7; when plotted in the Mo_{EF} vs U_{EF} diagram, they mostly fall between the $0.3\times(Mo/U)_{SW}$ and $3\times(Mo/U)_{SW}$ trend lines (Fig. 6). The data distribution looks similar for seep carbonates from the northern Congo fan (Hu et al., 2014), and suggests very dynamic redox conditions. High flux of hydrocarbon-rich fluids toward the seafloor likely generated a compressed vertical redox zonation within the sediments. Under such conditions, the $(Mo/U)_{EF}$ basically depends on the AOM rate: at relatively slow rate of hydrogen sulfide production, the threshold concentration for conversion of molybdate to thiomolybdate (Helz et al., 1996; Zheng et al., 2000) was unlikely to be achieved and therefore U accumulation prevailed over Mo, causing $(Mo/U)_{EF}$ <3.1. Enhanced AOM rates linked to higher CH_4 concentrations, on the contrary, progressively promoted sulfidic conditions within the SMTZ, resulting in $(Mo/U)_{EF}$ >3.1. No correlation between Mo_{EF} or U_{EF} and $^{87}Sr/^{86}Sr$ (Fig. 7) suggests that there is not a straightforward relation between the inception of strongly anoxic and/or

sulfidic conditions and the input of radiogenic fluids. The concomitant occurrence of Mo_{EF}>3.1, MREE enrichments and absence of positive Ce anomalies in some carbonates reflects the highly dynamic redox conditions during carbonate precipitation and supports the hypothesis of a compressed vertical geochemical zonation where the Fe-reduction zone partially overlaps the SO_4-reduction zone.

6. Conclusions

In this study, we characterized a carbonate outcrop formed in a fault-related seepage system (the Miocene Corella outcrop, northern Apennines, Italy) by radiogenic strontium isotopes ($^{87}Sr/^{86}Sr$), rare earth elements and Mo-U systematics to constrain fluid sources and reconstruct the seepage dynamics and redox conditions. Most of the samples formed in equilibrium with Langhian seawater, in agreement with the age of the host sediments. These findings confirm that the SIS methodology can be successfully applied to seep carbonates when the diagenetic alteration is negligible.

We also found evidence of the contribution of a deeper fluid source characterized by a highly radiogenic Sr isotope signature. This signal was recorded in carbonate phases precipitating in cavities and fractures and micrite from the conduit-rich facies at the base of the carbonate body, in conditions less influenced by seawater. This radiogenic signal likely derived from fluids that interacted with detrital clays of the underlying terrigenous turbidite successions, conveyed toward the seafloor by faults linked to the Apenninic deformational front.

Molybdenum and uranium enrichments in carbonates indicate an overall intense AOM and highly variable suboxic porewater conditions, episodically sulfidic. Although REE are very effective in representing temporal variations of redox conditions, they do not always adequately record the presence of a deeper fluid source due to mixing effects, and cannot effectively constrain the complexity of fault-controlled seepage systems.

With this study, we demonstrated that the integration of $^{87}Sr/^{86}Sr$ ratios and Mo-U systematics in ancient seep carbonates represents a novel and powerful approach to the investigation of fossil systems potentially allowing for more complete paleoenvironmental reconstructions. Extrapolating our results to modern seep carbonates, the combination of these

geochemical tracers can contribute to improve the understanding of the long-term evolution of modern seep systems in similar geotectonic settings and their role as a carbon sink.

Acknowledgments

This study was supported by a PostGrad Research Grant (Fall2017) of the International Association of Sedimentologists. Strontium isotope analyses have been facilitated through the Programma Giovani Ricercatori Rita Levi Montalcini to A. Cipriani. We thank Paola Iacumin, Antonietta Di Matteo and Enrico Maria Selmo of the University of Parma for analytical support during stable isotope analysis. We thank the anonymous reviewers for their comments and suggestions that greatly improved the manuscript.

References

Algeo, T.J., Tribovillard, N., 2009. Environmental analysis of paleoceanographic systems based on molybdenum–uranium covariation. Chem. Geol., 268(3-4), pp.211-225.

Aloisi, G., Pierre, C., Rouchy, J.M., Foucher, J.P., Woodside, J., 2000. Methane-related authigenic carbonates of eastern Mediterranean Sea mud volcanoes and their possible relation to gas hydrate destabilisation. Earth Planet. Sci. Lett., 184(1), pp.321-338.

Anderson, B., Bartlett, K.B., Frolking, S., Hayhoe, K., Jenkins, J.C., Salas, W.A., 2010. Methane and nitrous oxide emissions from natural sources. Office of Atmospheric Programs, US EPA, EPA 430-R-10-001, Washington DC.

Argentino, C., Reghizzi, M., Conti, S., Fioroni, C., Fontana, D., Salocchi, A., 2017. Strontium isotope stratigraphy as a contribution for dating Miocene shelf carbonates (s. Marino Fm., northern Apennines). Riv. It. Paleontol. Strat., vol. 123, pp. 39-50.

Argentino, C., Conti, S., Crutchley, G.J., Fioroni, C., Fontana, D., Johnson, J.E., 2019. Methane-derived authigenic carbonates on accretionary ridges: Miocene case studies in the northern Apennines (Italy) compared with modern submarine counterparts. Mar. Pet. Geol., 102, pp.860-872.

Argnani, A., Ricci Lucchi, F., 2001. Tertiary silicoclastic turbidite systems of the Northern Apennines. In Anatomy of an orogen: the Apennines and adjacent Mediterranean basins (pp. 327-349). Springer, Dordrecht.

Bayon, G., Birot, D., Ruffine, L., Caprais, J.C., Ponzevera, E., Bollinger, C., Donval, J.P., Charlou, J.L., Voisset, M., Grimaud, S., 2011. Evidence for intense REE scavenging at cold seeps from the Niger Delta margin. Earth Planet. Sci. Lett., 312(3-4), pp.443-452.

Birgel, D., Feng, D., Roberts, H.H., Peckmann, J., 2011. Changing redox conditions at cold seeps as revealed by authigenic carbonates from Alaminos Canyon, northern Gulf of Mexico. Chem. Geol., 285(1-4), pp.82-96.

Boetius A, Ravenschlag K, Schubert CJ, Rickert D, Widdel F, Gieseke A, Amann R, Jørgensen BB, Witte U, Pfannkuche O., 2000. A marine microbial consortium apparently mediating anaerobic oxidation of methane. Nature, 407(6804), 623.

Burke W.H., Denison R.E., Hetherington E.A., Koepnick R.B., Nelson H.F., Otto J.B., 1982. Variation of seawater the $^{87}Sr/^{86}Sr$ throughout Phanerozoic time. Geology, 10(10), pp.516-519.

Brand, U., Veizer, J., 1980. Chemical diagenesis of a multicomponent carbonate system--1: Trace elements. J. Sediment. Res., 50(4).

Campbell, K.A., 2006. Hydrocarbon seep and hydrothermal vent paleoenvironments and paleontology: Past developments and future research directions. Palaeogeogr. Palaeoclimatol. Palaeoecol., 232(2-4), pp.362-407.

Carminati, E., Doglioni, C., 2012. Alps vs. Apennines: The paradigm of a tectonically asymmetric Earth. Earth-Sci. Rev., 112(1-2), pp.67-96.

Chen, D.F., Huang, Y.Y., Yuan, X.L., Cathles III, L.M., 2005. Seep carbonates and preserved methane oxidizing archaea and sulfate reducing bacteria fossils suggest recent gas venting on the seafloor in the Northeastern South China Sea. Mar. Pet. Geol., 22(5), pp.613-621.

Chen, F., Hu, Y., Feng, D., Zhang, X., Cheng, S., Cao, J., Lu, H., Chen, D., 2016. Evidence of intense methane seepages from molybdenum enrichments in gas hydrate-bearing sediments of the northern South China Sea. Chem. Geol., 443, pp.173-181.

Collier, R.W., 1985. Molybdenum in the Northeast Pacific Ocean 1. Limnol. Oceanogr., 30(6), pp.1351-1354.

CONTI S., FONTANA D., MECOZZI S., PANIERI G., PINI G.A., 2010. LATE MIOCENE SEEP-CARBONATES AND FLUID MIGRATION ON TOP OF THE MONTEPETRA INTRABASINAL HIGH (NORTHERN APENNINES, ITALY): RELATIONS WITH SYNSEDIMENTARY FOLDING. SEDIMENTARY GEOLOGY, VOL. 231, P. 41-54

CONTI S, FIORONI, FONTANA D., GRILLENZONI C. (2016). DEPOSITIONAL HISTORY OF THE EPILIGURIAN WEDGE-TOP BASIN IN THE VAL MARECCHIA AREA (NORTHERN APENNINES, ITALY): A REVISION OF THE BURDIGALIAN-TORTONIAN SUCCESSION. ITALIAN JOURNAL OF GEOSCIENCES, VOL. 135(2), P. 324-335.

Conti, S., Fioroni, C., Fontana, D., 2017. Correlating shelf carbonate evolutive phases with fluid expulsion episodes in the foredeep (Miocene, northern Apennines, Italy). Mar. Pet. Geol., 79, pp.351-359.

Crusius, J., Calvert, S., Pedersen, T., Sage, D., 1996. Rhenium and molybdenum enrichments in sediments as indicators of oxic, suboxic and sulfidic conditions of deposition. Earth Planet. Sci. Lett., 145(1-4), pp.65-78.

Cumberland, S.A., Douglas, G., Grice, K., Moreau, J.W., 2016. Uranium mobility in organic matter-rich sediments: A review of geological and geochemical processes. Earth-Sci. Rev., 159, pp.160-185.

Denison, R.E., Koepnick, R.B., Fletcher, A., Howell, M.W., Callaway, W.S., 1994. Criteria for the retention of original seawater $^{87}Sr/^{86}Sr$ in ancient shelf limestones. Chem. Geol., 112(1-2), pp.131-143.

Dulski, P., 1994. Interferences of oxide, hydroxide and chloride analyte species in the determination of rare earth elements in geological samples by inductively coupled plasma-mass spectrometry. Fresen. J. Anal. Chem., 350(4-5), pp.194-203.

Elderfield, H., Upstill-Goddard, R., Sholkovitz, E.R., 1990. The rare earth elements in rivers, estuaries, and coastal seas and their significance to the composition of ocean waters. Geochim. Cosmochim. Acta , 54, pp. 971–991.

Emerson, S.R., Huested, S.S., 1991. Ocean anoxia and the concentrations of molybdenum and vanadium in seawater. Mar. Chem., 34(3-4), pp.177-196.

Erickson, B.E., Helz, G.R., 2000. Molybdenum (VI) speciation in sulfidic waters: stability and lability of thiomolybdates. Geochim. Cosmochim. Ac., 64(7), pp.1149-1158.

Feng, D., Chen, D., Peckmann, J., 2009a. Rare earth elements in seep carbonates as tracers of variable redox conditions at ancient hydrocarbon seeps. Terra Nova, 21(1), pp.49-56.

Feng, D., Chen, D., Roberts, H.H., 2009b. Petrographic and geochemical characterization of seep carbonate from Bush Hill (GC 185) gas vent and hydrate site of the Gulf of Mexico. Mar. Pet. Geol., 26(7), pp.1190-1198.

Feng, D., Chen, D., Peckmann, J., Bohrmann, G., 2010. Authigenic carbonates from methane seeps of the northern Congo fan: microbial formation mechanism. Mar. Pet. Geol., 27(4), pp.748-756.

Frimmel, H.E., 2010. On the reliability of stable carbon isotopes for Neoproterozoic chemostratigraphic correlation. Precambrian Res. 182, pp. 239–253.

Ge, L., Jiang, S.Y., Swennen, R., Yang, T., Yang, J.H., Wu, N.Y., Liu, J., Chen, D.H., 2010. Chemical environment of cold seep carbonate formation on the northern continental slope of South China Sea: evidence from trace and rare earth element geochemistry. Mar. Geol., 277(1-4), pp.21-30.

Ge, L., Jiang, S.Y., 2013. Sr isotopic compositions of cold seep carbonates from the South China Sea and the Panoche Hills (California, USA) and their significance in palaeooceanography. J. Asian Earth Sci., 65, pp.34-41.

Greinert, J., Bohrmann, G. and Suess, E., 2001. Gas hydrate- associated carbonates and methane- venting at Hydrate Ridge: classification, distribution, and origin of authigenic lithologies. In Paull, C.K. and Dillon, W.P. (Eds.), Natural gas hydrates: occurrence, distribution, and detection. American Geophysical Union Geophysical Monograph Series, Washington DC, 124, pp.99-113.

Haley, B.A., Klinkhammer, G.P., McManus, J., 2004. Rare earth elements in pore waters of marine sediments. Geochim. Cosmochim. Acta, 68(6), pp.1265-1279.

Helz, G.R., Miller, C.V., Charnock, J.M., Mosselmans, J.F.W., Pattrick, R.A.D., Garner, C.D., Vaughan, D.J., 1996. Mechanism of molybdenum removal from the sea and its concentration in black shales: EXAFS evidence. Geochim. Cosmochim. Acta, 60(19), pp.3631-3642.

Himmler, T., Bach, W., Bohrmann, G., Peckmann, J., 2010. Rare earth elements in authigenic methane-seep carbonates as tracers for fluid composition during early diagenesis. Chem. Geol., 277(1), pp.126-136.

Himmler, T., Haley, B.A., Torres, M.E., Klinkhammer, G.P., Bohrmann, G., Peckmann, J., 2013. Rare earth element geochemistry in cold-seep pore waters of Hydrate Ridge, northeast Pacific Ocean. Geo-Mar. Lett., 33(5), pp.369-379.

Hong, W.L., Torres, M.E., Portnov, A., Waage, M., Haley, B., Lepland, A., 2018. Variations in gas and water pulses at an Arctic seep: fluid sources and methane transport. Geophys. Res. Lett., 45(9), pp.4153-4162.

Hu, Y., Feng, D., Peckmann, J., Roberts, H.H., Chen, D., 2014. New insights into cerium anomalies and mechanisms of trace metal enrichment in authigenic carbonate from hydrocarbon seeps. Chem. Geol., 381, pp.55-66.

Hu, Y., Chen, L., Feng, D., Liang, Q., Xia, Z., Chen, D., 2017. Geochemical record of methane seepage in authigenic carbonates and surrounding host sediments: A case study from the South China Sea. J. Asian Earth Sci., 138, pp.51-61.

Jakubowicz, M., Dopieralska, J., Belka, Z., 2015. Tracing the composition and origin of fluids at an ancient hydrocarbon seep (Hollard Mound, Middle Devonian, Morocco): A Nd, REE and stable isotope study. Geochim. Cosmochim. Acta, 156, pp.50-74.

Jarvis, K.E., Gray, A.L., McCurdy, E., 1989. Avoidance of spectral interference on europium in inductively coupled plasma mass spectrometry by sensitive measurement of the doubly charged ion. J. Anal. Atom. Spectrom., 4(8), pp.743-747.

Jiang, S.Y., Zhao, H.X., Chen, Y.Q., Yang, T., Yang, J.H., Ling, H.F., 2007. Trace and rare earth element geochemistry of phosphate nodules from the lower Cambrian black shale sequence in the Mufu Mountain of Nanjing, Jiangsu province, China. Chem. Geol., 244(3-4), pp.584-604.

Jochum, K. P., Weis, U., Stoll, B., Kuzmin, D., Yang, Q., Raczek, I., Jacob, D. E., Stracke, A., Birbaum K., Frick, D. A., Günther, D., Enzweiler, J., 2011. Determination of reference values for NIST SRM 610–617 glasses following ISO guidelines. Geostand. Geoanal. Res., 35, pp. 397-429.

Joseph, C., Torres, M.E., Martin, R.A., Haley, B.A., Pohlman, J.W., Riedel, M., Rose, K., 2012. Using the $^{87}Sr/^{86}Sr$ of modern and paleoseep carbonates from northern Cascadia to link modern fluid flow to the past. Chem. Geol., 334, pp.122-130.

Joseph, C., Campbell, K.A., Torres, M.E., Martin, R.A., Pohlman, J.W., Riedel, M., Rose, K., 2013. Methane-derived authigenic carbonates from modern and paleoseeps on the Cascadia margin: Mechanisms of formation and diagenetic signals. Palaeogeogr., Palaeoclimatol., Palaeoecol., 390, pp.52-67.

Kiel, S., Hansen, B.T., 2015. Cenozoic methane-seep faunas of the Caribbean region. PloS one, 10(10), p.e0140788.

Kiel, S., Hansen, C., Nitzsche, K.N., Hansen, B.T., 2014. Using $^{87}Sr/^{86}Sr$ Ratios to Date Fossil Methane Seep Deposits: Methodological Requirements and an Example from the Great Valley Group, California. J. Geol., 122(4), pp.353-366.

Kim, J.H., Torres, M.E., Haley, B.A., Kastner, M., Pohlman, J.W., Riedel, M., Lee, Y.J., 2012. The effect of diagenesis and fluid migration on rare earth element distribution in pore fluids of the northern Cascadia accretionary margin. Chem. Geol., 291, pp.152-165.

Li, D., Shields-Zhou, G.A., Ling, H.F., Thirlwall, M., 2011. Dissolution methods for strontium isotope stratigraphy: Guidelines for the use of bulk carbonate and phosphorite rocks. Chem. Geol., 290(3-4), pp.133-144.

Li, N., Feng, D., Chen, L., Wang, H., Chen, D., 2016. Using sediment geochemistry to infer temporal variation of methane flux at a cold seep in the South China Sea. Mar. Pet. Geol., 77, pp.835-845.

Liang, Q., Hu, Y., Feng, D., Peckmann, J., Chen, L., Yang, S., Liang, J., Tao, J., Chen, D., 2017. Authigenic carbonates from newly discovered active cold seeps on the northwestern slope of the South China Sea: Constraints on fluid sources, formation environments, and seepage dynamics. Deep Sea Res. Pt I, 124, pp.31-41.

MacRae, N.D., Nesbitt, H.W., Kronberg, B.I., 1992. Development of a positive Eu anomaly during diagenesis. Earth Planet. Sci. Lett., 109(3-4), pp.585-591.

Magyar, B., Moor, H.C., Sigg, L., 1993. Vertical distribution and transport of molybdenum in a lake with a seasonally anoxic hypolimnion. Limnol. Oceanogr., 38(3), pp.521-531.

Malone, M.J., Claypool, G., Martin, J.B., Dickens, G. R., 2002. Variable methane fluxes in shallow marine systems over geologic time: The composition and origin of pore waters and authigenic carbonates on the New Jersey shelf. Mar. Geol., 189(3), 175-196.

McArthur, J.M., Howarth, R.J. Bailey, T.R., 2001. Strontium isotope stratigraphy: LOWESS version 3: best fit to the marine Sr-isotope curve for 0–509 Ma and accompanying look-up table for deriving numerical age. J. Geol., 109(2), pp.155-170.

McArthur, J.M., Howarth, R.J., Shields, G.A., 2012. Strontium isotope stratigraphy. In Gradstein, F.M., Ogg, J.G., Schmitz, M., Ogg, G. (Eds.). The geologic time scale 2012. Amsterdam, Elsevier, pp. 127-144.

Meyer, E.E., Quicksall, A.N., Landis, J.D., Link, P.K., Bostick, B.C., 2012. Trace and rare earth elemental investigation of a Sturtian cap carbonate, Pocatello, Idaho: Evidence for ocean redox conditions before and during carbonate deposition. Precambrian Res., 192, pp.89-106.

Morford, J.L., Emerson, S.R., Breckel, E.J., Kim, S.H., 2005. Diagenesis of oxyanions (V, U, Re, and Mo) in pore waters and sediments from a continental margin. Geochim. Cosmochim. Acta, 69(21), pp.5021-5032.

Morford, J.L., Martin, W.R., François, R., Carney, C.M., 2009. A model for uranium, rhenium, and molybdenum diagenesis in marine sediments based on results from coastal locations. Geochim. Cosmochim. Acta, 73(10), pp.2938-2960.

Naehr, T.H., Rodriguez, N.M., Bohrmann, G., Paull, C.K., Botz, R., 2000. Methane derived authigenic carbonates associated with gas hydrate decomposition and fluid venting above the Blake Ridge Diapir. In Proceedings of the Ocean Drilling Program, Scientific Results, Vol. 164, pp. 285-300.

Naehr, T. H., Eichhubl, P., Orphan, V. J., Hovland, M., Paull, C. K., Ussler III, W., Lorenson, D. T., Greene, H. G., 2007. Authigenic carbonate formation at hydrocarbon seeps in continental margin sediments: a comparative study. Deep Sea Res. Pt. II, 54(11-13), 1268-1291.

Okai, T., Suzuki, A., Terashima, S., Inoue, M., Nohara, M., Kawahata, H., Imai, N., 2004. Collaborative analysis of GSJ/AIST Geochemical Reference Materials JCp-1 (Coral) and JCt-1 (Giant Clam). Chikyu Kagaku. Geochemistry, 38 (4), 281–286.

Olivarez, A.M., Owen, R.M., 1991. The europium anomaly of seawater: implications for fluvial versus hydrothermal REE inputs to the oceans. Chem. Geol., 92(4), pp.317-328.

Pearce, N.J., Perkins, W.T., Westgate, J.A., Gorton, M.P., Jackson, S.E., Neal, C.R., Chenery, S.P., 1997. A compilation of new and published major and trace element data for NIST SRM 610 and NIST SRM 612 glass reference materials. Geostand. Geoanal. Res., 21(1), pp.115-144.

Peckmann, J., Reimer, A., Luth, U., Luth, C., Hansen, B.T., Heinicke, C., Hoefs, J., Reitner, J., 2001. Methane-derived carbonates and authigenic pyrite from the northwestern Black Sea. Mar. Geol., 177(1-2), pp.129-150.

Pierre, C., Bayon, G., Blanc-Valleron, M.M., Mascle, J., Dupré, S., 2014. Authigenic carbonates related to active seepage of methane-rich hot brines at the Cheops mud volcano, Menes caldera (Nile deep-sea fan, eastern Mediterranean Sea). Geo-Mar. Lett., 34(2-3), pp.253-267.

Qi, L., Zhou, M.F., Malpas, J., Sun, M., 2005. Determination of Rare Earth Elements and Y in Ultramafic Rocks by ICP- MS After Preconcentration Using $Fe(OH)_3$ and $Mg(OH)_2$ Coprecipitation. Geostand. Geoanal. Res., 29(1), pp.131-141.

Ricci Lucchi, F., 1986. The Oligocene to Recent foreland basins of the northern Apennines. Foreland basins, pp.103-139.

Roberts, H.H., 2001. Fluid and Gas Expulsion on the Northern Gulf of Mexico Continental Slope: Mud- Prone to Mineral- Prone Responses. In Paull, C.K. and Dillon, W.P. (Eds.), Natural gas hydrates: occurrence, distribution, and detection. American Geophysical Union Geophysical Monograph Series, Washington DC, 124, pp.145-161.

Russell, A.D., Emerson, S., Nelson, B.K., Erez, J., Lea, D.W., 1994. Uranium in foraminiferal calcite as a recorder of seawater uranium concentrations. Geochim. Cosmochim. Acta, 58(2), pp.671-681.

Sample, J.C., Reid, M.R., Tols, H.J., Moore, J.C., 1993. Carbonate cements indicate channeled fluid flow along a zone of vertical faults at the deformation front of the Cascadia accretionary wedge (northwest US coast). Geology, 21(6), pp.507-510.

Sarkar, A., Sarangi, S., Ebihara, M., Bhattacharya, S.K., Ray, A.K., 2003. Carbonate geochemistry across the Eocene/Oligocene boundary of Kutch, western India: implications to oceanic O2 -poor condition and foraminiferal extinction. Chem. Geol. 201, 281–293.

Scott, C., Lyons, T.W., 2012. Contrasting molybdenum cycling and isotopic properties in euxinic versus non-euxinic sediments and sedimentary rocks: Refining the paleoproxies. Chem. Geol., 324, pp.19-27.

Shields, G., Stille, P., 2001. Diagenetic constraints on the use of cerium anomalies as palaeoseawater redox proxies: an isotopic and REE study of Cambrian phosphorites. Chem. Geol., 175(1-2), pp.29-48.

Shields, G., Webb, G.E., 2004. Has the REE composition of seawater changed over geological time?. Chem. Geol., 204(1-2), pp.103-107.

Solomon E.A., Kastner M., Wheat C.G., Jannasch H., Robertson G., Davis, E.E., Morris, J.D., 2009. Long-term hydrogeochemical records in the oceanic basement and forearc prism at the Costa Rica subduction zone. Earth Planet. Sci. Lett., 282(1), pp.240-251.

Sturchio, N.C., Antonio, M.R., Soderholm, L., Sutton, S.R., Brannon, J.C., 1998. Tetravalent uranium in calcite. Science 281 (5379), 971–973.

Taylor, S.R., McLennan, S.M., 1985. The continental crust: its composition and evolution. Oxford: Blackwell Press, 1, p.312.

Teichert, B.M.A., Torres, M.E., Bohrmann, G., Eisenhauer, A., 2005. Fluid sources, fluid pathways and diagenetic reactions across an accretionary prism revealed by Sr and B geochemistry. Earth Planet. Sci. Lett., 239(1), pp.106-121.

Thirlwall, M.F., 1991. Long-term reproducibility of multicollector Sr and Nd isotope ratio analysis. Chem. Geol.: Isotope Geoscience section, 94(2), pp.85-104.

Tinterri, R., Magalhaes, P.M., 2011. Synsedimentary structural control on foredeep turbidites: An example from Miocene Marnoso-arenacea Formation, Northern Apennines, Italy. Mar. Pet. Geol., 28(3), pp.629-657.

Tong, H., Feng, D., Cheng, H., Yang, S., Wang, H., Min, A.G., Edwards, R.L., Chen, Z., Chen, D., 2013. Authigenic carbonates from seeps on the northern continental slope of the South China Sea: new insights into fluid sources and geochronology. Mar. Pet. Geol., 43, pp.260-271.

Torres, M.E., Teichert, B.M.A., Trehu, A.M., Borowski, W., Tomaru, H., 2004. Relationship of pore water freshening to accretionary processes in the Cascadia margin: fluid sources and gas hydrate abundance. Geophys. Res. Lett., 31(22).

Tostevin, R., Shields, G.A., Tarbuck, G.M., He, T., Clarkson, M.O., Wood, R.A., 2016. Effective use of cerium anomalies as a redox proxy in carbonate-dominated marine settings. Chem. Geol., 438, pp.146-162.

Tran, T.H., Kato, K., Wada, H., Fujioka, K., Matsuzaki, H., 2014. Processes involved in calcite and aragonite precipitation during carbonate chimney formation on Conical Seamount, Mariana forearc: evidence from geochemistry and carbon, oxygen, and strontium isotopes. J.Geochem. Explor., 137, pp.55-64.

Tribovillard, N., Riboulleau, A., Lyons, T., Baudin, F., 2004. Enhanced trapping of molybdenum by sulfurized organic matter of marine origin as recorded by various Mesozoic formations. Chem. Geol. 213, 385–401.

Tribovillard, N., Algeo, T.J., Lyons, T., Riboulleau, A., 2006. Trace metals as paleoredox and paleoproductivity proxies: an update. Chem. Geol., 232(1-2), pp.12-32.

Tribovillard, N., Du Châtelet, E.A., Gay, A., Barbecot, F., Sansjofre, P., Potdevin, J.L., 2013. Geochemistry of cold seepage-impacted sediments: Per-ascensum or per-descensum trace metal enrichment?. Chem. Geol., 340, pp.1-12.

Tucker, M.E., Wright, V.P. 1990. Carbonate sedimentology. Blackwell Scientific Publications, Oxford, 482p.

Veizer, J., 1989. Strontium isotopes in seawater through time. Annu. Rev. Earth Pl. Sc., 17(1), pp.141-167.

Vescogni, A., Bosellini, F.R., Cipriani, A., Gürler, G., Ilgar, A., Paganelli, E., 2014. The Dağpazarı carbonate platform (Mut Basin, Southern Turkey): Facies and environmental reconstruction of a coral reef system during the Middle Miocene Climatic Optimum. Palaeogeogr., palaeoclimatol., palaeoecol., 410, pp.213-232.

Viola, I., Capozzi, R., Bernasconi, S.M., Rickli, J., 2017. Carbon, oxygen and strontium isotopic constraints on fluid sources, temperatures and biogeochemical processes during the formation of seep carbonates-Secchia River site, Northern Apennines. Sediment. Geol., 357, pp.1-15.

Wang, S., Yan, W., Chen, Z., Zhang, N., Chen, H., 2014. Rare earth elements in cold seep carbonates from the southwestern Dongsha area, northern South China Sea. Mar. Pet. Geol., 57, pp.482-493.

Wang, S., Magalhães, V.H., Pinheiro, L.M., Liu, J., Yan, W., 2015. Tracing the composition, fluid source and formation conditions of the methane-derived authigenic carbonates in the Gulf of Cadiz with rare earth elements and stable isotopes. Mar. Pet. Geol., 68, pp.192-205.

Wang, Q., Tong, H., Huang, C.Y. Chen, D., 2018. Tracing fluid sources and formation conditions of Miocene hydrocarbon-seep carbonates in the central Western Foothills, Central Taiwan. J. Asian Earth Sci., 168, pp. 186-196.

Wang, Q., Chen, D., Peckmann, J., 2019. Iron shuttle controls on molybdenum, arsenic, and antimony enrichment in Pliocene methane-seep carbonates from the southern Western Foothills, Southwestern Taiwan. Mar. Pet. Geol., 100, pp.263-269.

Weber, M., Lugli, F., Jochum, K.P., Cipriani, A., Scholz, D., 2018. Calcium carbonate and phosphate reference materials for monitoring bulk and microanalytical determination of Sr isotopes. Geostand. Geoanal. Res., 42(1), pp.77-89.

Wright, J., Schrader, H., Holser, W.T., 1987. Paleoredox variations in ancient oceans recorded by rare earth elements in fossil apatite. Geochim. Cosmochim. Acta, 51(3), pp.631-644.

Zachos, J., Pagani, M., Sloan, L., Thomas, E., Billups, K., 2001. Trends, rhythms, and aberrations in global climate 65 Ma to present. Science, 292(5517), pp.686-693.

Zheng, Y., Anderson, R.F., van Geen, A., Kuwabara, J., 2000. Authigenic molybdenum formation in marine sediments: a link to pore water sulfide in the Santa Barbara Basin. Geochim. Cosmochim. Acta, 64(24), pp.4165-4178.

Zwicker, J., Smrzka, D., Himmler, T., Monien, P., Gier, S., Goedert, J.L., Peckmann, J., 2018. Rare earth elements as tracers for microbial activity and early diagenesis: A new perspective from carbonate cements of ancient methane-seep deposits. Chem. Geol., 501, pp.77-85.

CAPTIONS

Fig. 1. A) Simplified geological map of the northern Apennines showing the main structural units (different colors) and location of the Corella seep carbonate outcrop (star symbol) (modified from Argentino et al., 2019). B) Distribution of authigenic seep carbonate bodies and stratigraphic and structural relationships with surrounding units. Carbonate bodies were named from L1 to L6. C) Structural sketch of the northern Apennine accretionary wedge/foredeep during the Middle Miocene. Corella seep located on the thrust-related anticline is indicated by the black star.

Fig. 2. A) Microphotograph showing dark gray matrix micrite (mm) enclosing fine siliciclastic grains, cloudy rim cement lining a cavity (rc) and limpid blocky calcite (bc) filling the center of the cavity, not considered in this study as related to late diagenesis (sample 15). B) Cloudy calcite cement filling a conduit (cc) within the micrite. Micrite and conduit filling are cut by late sparry calcite (sample condA). Scale bar = 1 mm

Fig. 3. Sample distribution on the seep carbonate bodies and resulting $^{87}Sr/^{86}Sr$ values for the different carbonate components. The Corella body (L1) is shown in detail, as it was more densely sampled.

Fig. 4. A) Sr versus Mn contents in the Corella seep carbonate samples. B) $^{87}Sr/^{86}Sr$ ratios plotted against Mn and Sr contents. $^{87}Sr/^{86}Sr$ and Mn show no correlation. A strong correlation (R^2=0.88) is evident between $^{87}Sr/^{86}Sr$ and Sr values in rim cements. C) Stable carbon and oxygen isotopic compositions of micrite matrix and rim cements. D) Plot of $^{87}Sr/^{86}Sr$ versus $\delta^{13}C$ (left) and $\delta^{18}O$ (right).

Fig. 5. Strontium isotope data for the examined authigenic carbonates plotted on the seawater Sr curve of McArthur et al. (2012). Most micritic samples show $^{87}Sr/^{86}Sr$ ratios corresponding to Langhian seawater Sr composition (specifically MNN5a biozone, red square). Sr isotope composition of the rim cements has no age implication, but here they are used to highlight deviations from coeval seawater. Note that the most radiogenic samples, 3M, 3V and L2COR1VB are out of scale, not included in this figure.

Fig. 6. Rare earth element geochemistry of the Corella seep carbonates. A) PAAS-normalized REE patterns of micritic samples and calcite cements. B) Ce/Ce* vs. Pr/Pr* diagram of the Corella samples (after Bau and Dulski,1996). Field I: no Ce anomaly; Field IIa: unreal negative Ce anomaly caused by a positive La anomaly; Field IIb: unreal positive Ce anomaly caused by a negative La anomaly; Field IIIa: real positive Ce anomaly; Field IIIb: real negative Ce anomaly. Feld IV: positive Ce anomaly masked by a positive La anomaly.

Fig. 7. Mo_{EF} vs. U_{EF} for the Miocene seep carbonates of this study. The diagonal solid line represents the Mo/U molar ratio ~ 3.1 of modern seawater (1×SW; Algeo and Tribovillard, 2009) whereas dotted lines are fractions of it (3×SW, 0.3×SW, 0.1×SW). Colors refer to the Sr isotopic composition of carbonates as in Fig. 3.

Fig. 8. A) Ce/Ce* values plotted against the PAAS-normalized Dy_N/Sm_N ratio and total ΣREE: the lack of correlation indicates that carbonates preserved the original REE composition. B) Eu/Eu* vs. Ba/Sm diagram in micrites shows no correlation suggesting that the Eu anomalies did not derive from Ba interference during ICP-MS analysis; rim cements show a positive correlation by ($R^2 = 0.90$).

Fig. 9. Arsenic enrichments in the studied carbonate samples. A) As_{EF} vs. Mo_{EF} diagram indicates a moderate correlation (R^2=0.67). B) As_{EF} and Fe/Al ratios do not correlate (R^2<0.1) therefore we can rule out the "particulate shuttle hypothesis" (Tribovillard et al., 2013) as an explanation for strong Mo, U and As enrichments in our samples.

Tab. 1. Manganese and strontium contents and Sr isotopic composition of the Corella seep carbonates.

Tab 2. Stable carbon and oxygen isotopic composition of matrix micrite and rim cement.

Tab 3. Rare earth element content (mg/kg), Ce/Ce*, Eu/Eu*, Pr/Pr*, La/La* and Ba/Sm in the Corella seep carbonates.

Tab 4. Mo, U and As content (mg/kg) in the Corella seep carbonates and corresponding enrichment factors Mo_{EF}, U_{EF} and As_{EF}.

Tab.1 Mn and Sr contents and Sr isotopic results of the Corella seep carbonates.

Sample	Authigenic body	Material	Sr (mg/kg)	Mn (mg/kg)	$^{87}Sr/^{86}Sr$	2SE	Lower age (Ma)	Mean age (Ma)	Upper age (Ma)
1	L1	Mm	468	90	0.708755 (14)	0.000006	15.8	15.6	15.3
2VA	L1	Rc	916	98	0.708939 (15)	0.000005	8.8	7.5	6.8
2VB	L1	Rc	951	126	0.708949 (15)	0.000004	8.2	7.1	6.5
2M	L1	Mm	820	143	0.708787 (16)	0.000008	15.4	15.0	14.0
3M	L1	Mm	543	87	0.709132 (15)	0.000003	1.4	1.1	0.8
3V	L1	Rc	2285	115	0.709132 (15)	0.000005	1.4	1.1	0.8
8	L1	Mm	579	93	0.708781 (14)	0.000006	15.5	15.1	14.7
10	L1	Mm	541	44	0.708800 (14)	0.000006	15.1	14.6	13.1
15V	L1	Rc	494	34	0.708761 (15)	0.000005	15.8	15.5	15.2
15M	L1	Mm	328	116	0.708659 (16)	0.000006	17.1	16.9	16.7
16	L1	Mm	242	125	0.708783 (14)	0.000006	15.4	15.1	14.6
18	L1	Mm	267	151	0.708790 (14)	0.000006	15.3	14.8	14.0
19	L1	Mm	341	139	0.708769 (13)	0.000005	15.6	15.4	15.0
21M	L1	Mm	340	191	0.708728 (15)	0.000005	16.2	16.0	15.7
21B	L1	Mm	332	158	0.708713 (16)	0.000006	16.5	16.2	15.9
23	L1	Mm	298	133	0.708763 (14)	0.000006	15.7	15.5	15.1
24	L1	Mm	395	184	0.708786 (14)	0.000006	15.4	15.0	14.4
28	L1	Mm	399	113	0.708808 (14)	0.000006	14.9	14.0	12.7
30	L1	Mm	558	118	0.708765 (15)	0.000008	15.7	15.4	15.1
CondA_V	L1	Rc	382	118	0.708840 (15)	0.000005	13.0	11.8	11.0
CondA_M	L1	Mm	293	181	0.708768 (18)	0.000010	15.7	15.4	14.9
L2_VA	L2	Rc	450	59	0.708894 (15)	0.000003	10.3	9.7	9.0
L2_VB	L2	Rc	1686	236	0.709078 (16)	0.000006	3.5	2.2	1.8
L2_M	L2	Mm	1662	67	0.708837 (15)	0.000006	13.1	12.0	11.1
L2_G	L2	Shell	943	77	0.708802 (15)	0.000005	15.1	14.5	12.9
L4	L4	Mm	614	178	0.708980 (13)	0.000005	6.7	6.2	5.9
L4*	L4	Mm	368	145	0.708875 (13)	0.000005	11.0	10.4	9.8
L5	L5	Mm	435	161	0.708847 (15)	0.000008	12.6	11.5	10.7
L5_V	L5	Rc	533	176	0.708851	0.000006	12.3	11.3	10.6

Note: maximum and minimum ages are obtained by subtracting and summing the cumulative error (reported in parenthesis) to mean isotopic value, and converted using the Look-up Table 5 (McArthur et al., 2012). The double standard error (2SE) refers to the internal analytical error of each measurement. Mm: Matrix micrite; Rc: Rim cement; Shell= Lucinid shell.

Tab.2 Carbon and Oxygen stable isotope composition of seep carbonates from the examined outcrop.

Sample	Component	$\delta^{13}C$ (‰ VPDB)	$\delta^{18}O$ (‰ VPDB)
3M	Mm	-26.6	-1.9
3V	Rc	-28.4	-8.0
L2_M	Mm	-31.6	-2.6
L2_VA	Rc	-29.2	-3.9
L2_VB	Rc	-28.8	-7.2
L4	Mm	-27.8	-2.6
L5	Mm	-27.4	-2.8
L5_V	Rc	-25.7	-4.0
CondA_M	Mm	-34.1	0.3
CondA_V	Rc	-38.7	-0.2

Mm: Matrix micrite; Rc: Rim cement.

2Mb	3M	3V	8	10	15V	15M	16	18	19	21M	21B	23	24	28	30	CondAV	CondAM	L2VA	L2VB	L2M
2.18	2.38	1.08	2.36	2.02	0.25	2.72	3.29	3.48	3.1	2.87	2.74	2.51	2.44	2.50	2.30	3.53	2.73	0.03	0.20	3.05
6.17	5.02	1.59	4.48	3.14	0.37	6.16	4.09	5.95	4.3	6.87	6.65	4.32	3.87	6.26	4.03	5.98	4.10	0.05	0.27	3.31
0.74	0.62	0.18	0.63	0.38	0.04	0.74	0.50	0.71	0.5	0.81	0.77	0.50	0.44	0.72	0.48	0.65	0.49	0.01	0.03	0.40
2.88	2.43	0.82	2.51	1.51	0.17	2.86	1.95	2.77	2.0	3.17	2.98	1.94	1.74	2.83	1.90	2.50	1.94	0.03	0.14	1.61
0.61	0.50	0.18	0.51	0.31	0.03	0.61	0.42	0.58	0.4	0.66	0.61	0.41	0.36	0.58	0.38	0.50	0.41	0.01	0.03	0.31
0.15	0.14	0.04	0.15	0.10	0.01	0.17	0.13	0.16	0.1	0.18	0.16	0.11	0.11	0.17	0.12	0.13	0.11	<0.01	0.01	0.12
0.68	0.57	0.17	0.56	0.35	0.03	0.67	0.46	0.66	0.5	0.75	0.70	0.45	0.41	0.66	0.44	0.39	0.48	0.01	0.03	0.35
0.10	0.08	0.03	0.08	0.05	<0.01	0.10	0.07	0.10	0.1	0.11	0.10	0.07	0.06	0.10	0.06	0.07	0.07	<0.01	<0.01	0.05
0.59	0.51	0.17	0.47	0.31	0.03	0.61	0.43	0.61	0.5	0.68	0.62	0.40	0.36	0.60	0.38	0.39	0.42	0.01	0.02	0.28
0.12	0.11	0.04	0.10	0.06	0.01	0.12	0.09	0.12	0.1	0.14	0.13	0.08	0.07	0.12	0.08	0.09	0.09	<0.01	<0.01	0.06
0.33	0.32	0.11	0.28	0.19	0.02	0.35	0.25	0.36	0.3	0.42	0.38	0.24	0.22	0.36	0.24	0.26	0.25	<0.01	0.01	0.17
0.05	0.05	0.01	0.04	0.03	<0.01	0.05	0.04	0.05	0.0	0.06	0.06	0.04	0.03	0.05	0.04	0.05	0.04	<0.01	<0.01	0.02
0.26	0.28	0.09	0.24	0.16	0.01	0.30	0.22	0.31	0.2	0.39	0.35	0.22	0.19	0.33	0.22	0.32	0.22	<0.01	0.01	0.14
0.04	0.05	0.01	0.04	0.03	<0.01	0.05	0.03	0.05	0.0	0.06	0.06	0.04	0.03	0.05	0.04	0.05	0.03	<0.01	<0.01	0.02
14.91	13.04	4.5	12.44	8.63	1.0	15.50	11.97	15.93	12.1	17.18	16.32	11.33	10.34	15.35	10.72	14.9	11.36	0.1	0.8	9.89
1.2	1.0	0.7	0.8	0.8	0.8	1.0	0.7	0.8	0.7	1.1	1.1	0.9	0.8	1.1	0.9	0.9	0.8	0.8	0.7	0.6
1.1	1.2	1.1	1.3	1.5	1.7	1.2	1.4	1.2	1.3	1.2	1.1	1.2	1.3	1.2	1.4	1.4	1.2	2.6	1.2	1.8
1.0	1.0	0.9	1.1	1.0	0.9	1.0	1.0	1.0	1.0	1.0	1.0	1.0	1.0	1.0	1.0	1.0	1.0	0.8	0.9	1.0
0.7	0.9	2.4	0.9	1.3	2.2	0.9	1.6	1.2	1.4	0.9	0.8	1.2	1.3	0.8	1.2	1.3	1.3	6.4	2.9	2.0
276.8	323.6	70.6	713.4	979.6	6116	326.6	667.5	447.5	745.2	271.9	386.1	400.1	427.0	362.1	977.2	386.2	460.9	13302	2692	504.8

Tab 3. Rare earth element content (mg/kg), Ce/Ce*, Eu/Eu*, Pr/Pr*, La/La* and Ba/Sm in the Corella seep carbonates.

Tab 4. Mo, U and As content (mg/kg) in the Corella seep carbonates and corresponding enrichment factors Mo_{EF}, U_{EF} and As_{EF}.

Sample	Mo (mg/kg)	U (mg/kg)	Mo_{EF}	U_{EF}	As (mg/kg)	As_{EF}	Fe/Al

1	6.7	3.2	59.4	15.5	2.6	23.1	0.59
2VA	<0.1	0.4	n.d.	n.d.	n.d.	n.d.	n.d.
2VB	<0.1	1.4	n.d.	n.d.	n.d.	n.d.	n.d.
2Mb	4.6	3.2	88.4	32.9	n.d.	n.d.	1.36
3M	34.4	9.4	233.5	34.1	n.d.	n.d.	0.65
3V	0.4	0.2	n.d.	n.d.	n.d.	n.d.	n.d.
8	4.6	1.4	40.7	6.7	1.7	15.1	0.61
10	11.9	2.3	131.4	13.6	3.2	35.0	0.60
15V	3.0	0.2	n.d.	n.d.	n.d.	n.d.	n.d.
15M	3.7	4.0	18.3	10.8	n.d.	n.d.	0.60
16	4.9	2.0	26.5	5.8	1.4	7.4	0.58
18	2.3	0.8	12.0	2.4	1.2	6.0	0.54
19	6.1	4.1	47.1	17.0	1.4	10.6	0.60
21M	7.4	4.0	30.2	8.8	n.d.	n.d.	0.60
21B	12.0	5.2	44.8	10.4	n.d.	n.d.	0.57
23	7.9	2.3	53.2	8.3	3.8	25.9	0.58
24	4.6	1.3	33.7	5.0	1.7	12.4	0.59
28	4.1	3.7	28.5	13.7	0.5	3.8	0.69
30	9.7	7.5	130.7	54.2	1.6	21.5	0.69
CondA_V	0.3	0,6	n.d.	n.d.	n.d.	n.d.	n.d.
CondA_M	4.6	3.3	33.0	12.7	n.d.	n.d.	0.55
L2_VA	<0.1	<0.1	n.d.	n.d.	n.d.	n.d.	n.d.
L2_VB	<0.1	<0.1	n.d.	n.d.	n.d.	n.d.	n.d.
L2_M	1.7	4.5	60.1	86.6	n.d.	n.d.	1.11
L2_G	0.6	0.8	n.d.	n.d.	n.d.	n.d.	n.d.
L4	0.6	0.2	4.4	0.9	0.2	1.5	0.61
L4*	9.1	3.0	48.2	8.4	4.0	21.5	0.61
L5	1.3	0.9	19.0	6.7	1.0	14.8	0.75
L5_V	0.9	0.6	n.d.	n.d.	0.3	n.d.	n.d.

Note: $X_{EF} = [(X / Al)_{sample} / (X / Al)_{PAAS}]$, samples are normalized using the Post Archean Australian Shale compositions (Taylor and McLennan, 1985). The authigenic fraction of Fe is expressed as Fe/Al ratio. n.d.: no data.

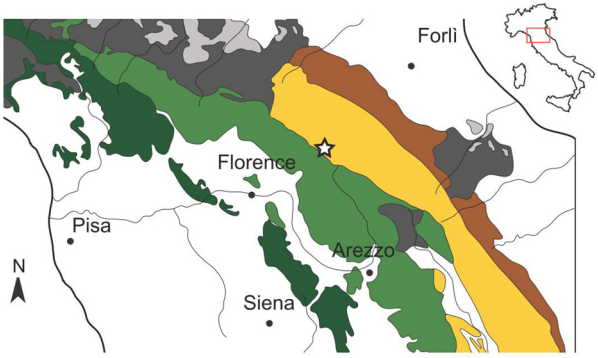

A

50 km

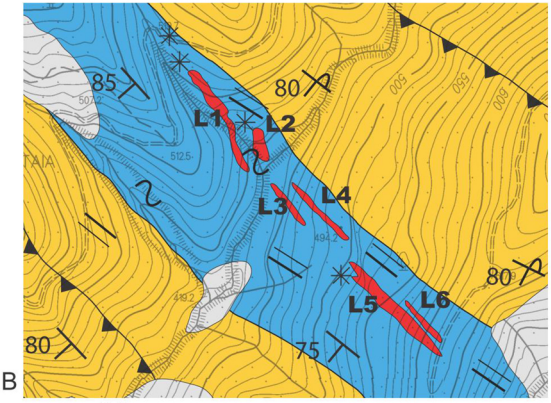

B

250 m

Northern Apennines

Epiligurian units (Upper Eocene-Lower Pliocene)

Ligurian-subligurian units (Upper Cretaceous-Oligocene)

Tuscan units

Outer Tuscan units (Paleogene-Middle Miocene)

Inner Tuscan units (Trias-Lower Miocene)

Studied outcrop

Vertical bedding

80 Strike and dip of bedding

80 Overturned bedding

Soft-sediment deformation

Thrust

Seep carbonates

Meter-sized seep carbonate blocks

Umbro-Marchean units

Outer Marnoso-arenacea Fm (Middle-Upper Miocene)

Inner Marnoso-arenacea Fm (Lower-Middle Miocene)

Pelitic stratigraphic interval (Langhian)

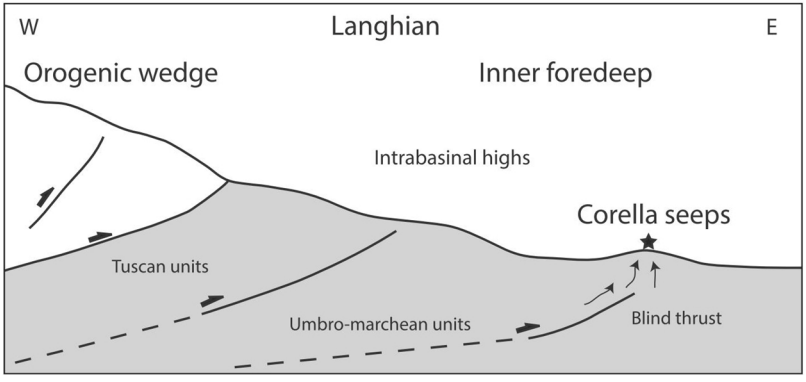

C

Thrust fault

Inferred fluid migration pathways

Figure 1

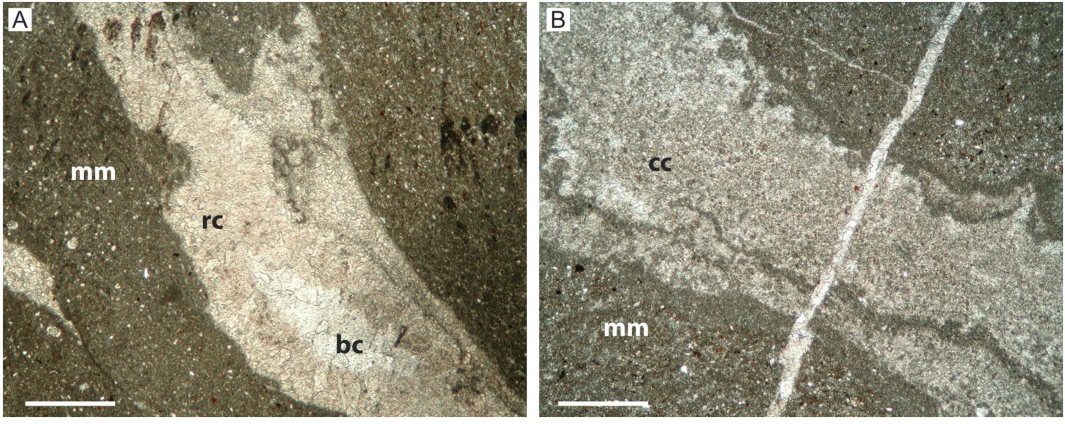

Figure 2

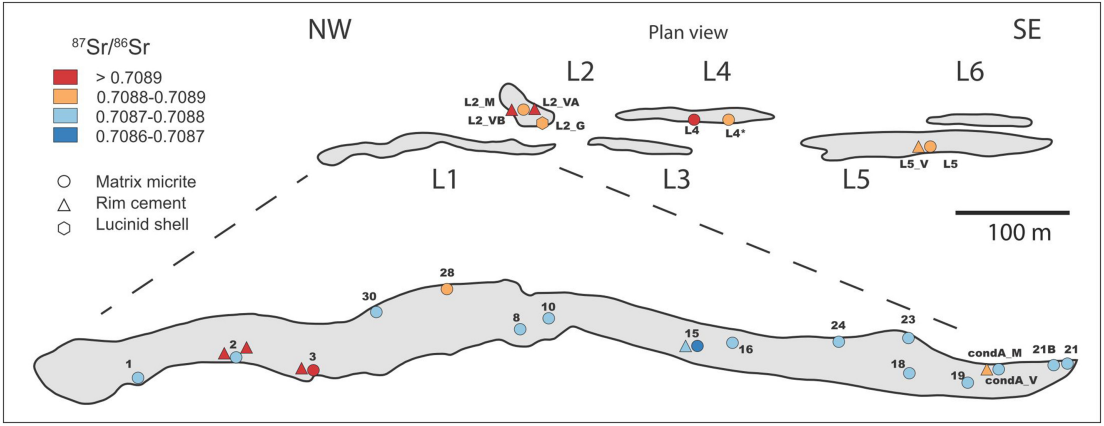
NW
Plan view
SE
87Sr/86Sr
> 0.7089
0.7088-0.7089
0.7087-0.7088
0.7086-0.7087
Matrix micrite
Rim cement
Lucinid shell
L2
L4
L6
L2_M
L2_VA
L2_VB
L2_G
L4
L4*
L1
L3
L5
L5_V
L5
100 m
1
2
3
30
28
8
10
15
16
24
23
18
19
condA_M
condA_V
21B
21

Figure 3

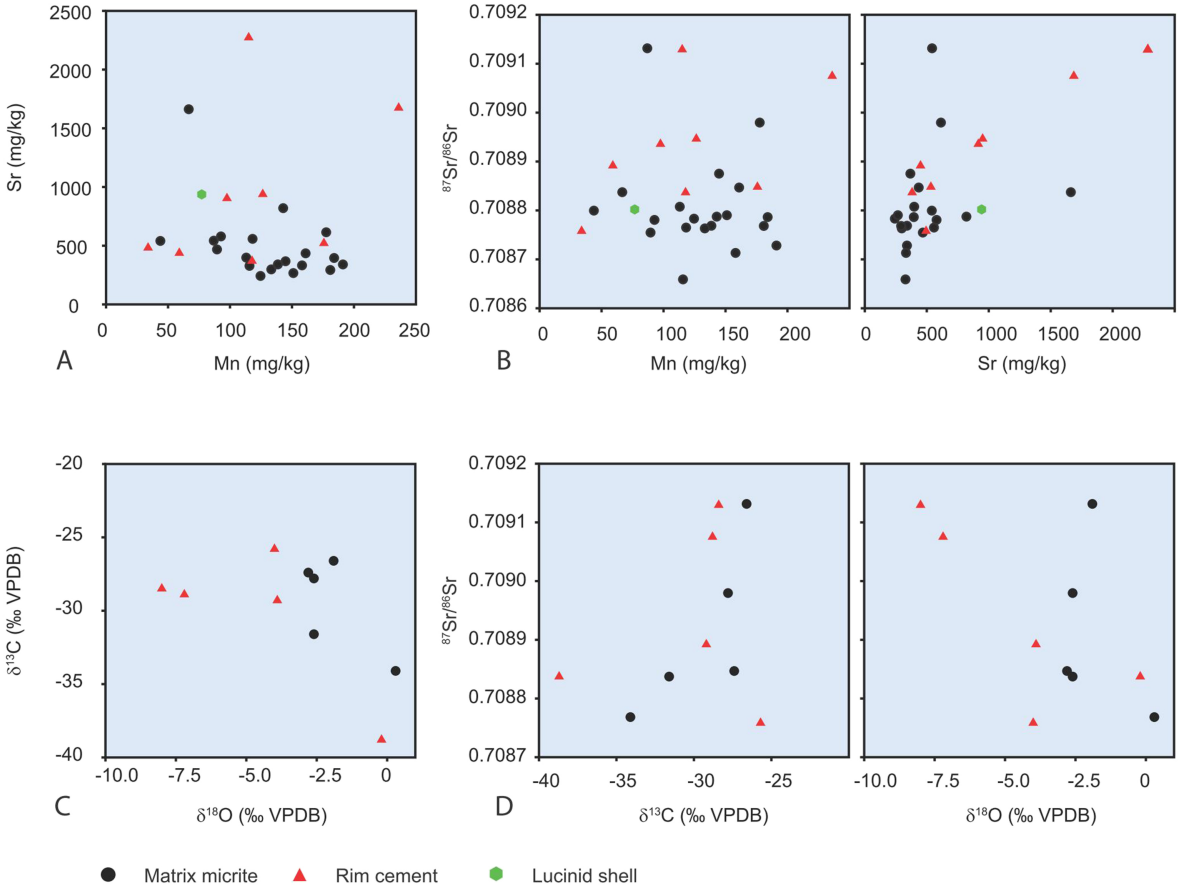
Sr (mg/kg)
2500
2000
1500
1000
500
0
0
50
100
150
200
250
Mn (mg/kg)
A
$^{87}Sr/^{86}Sr$
0.7092
0.7091
0.7090
0.7089
0.7088
0.7087
0.7086
0
50
100
150
200
Mn (mg/kg)
0
500
1000
1500
2000
Sr (mg/kg)
B
$\delta^{13}C$ (‰ VPDB)
-20
-25
-30
-35
-40
-10.0
-7.5
-5.0
-2.5
0
$\delta^{18}O$ (‰ VPDB)
C
$^{87}Sr/^{86}Sr$
0.7092
0.7091
0.7090
0.7089
0.7088
0.7087
-40
-35
-30
-25
$\delta^{13}C$ (‰ VPDB)
-10.0
-7.5
-5.0
-2.5
0
$\delta^{18}O$ (‰ VPDB)
D
Matrix micrite
Rim cement
Lucinid shell

Figure 4

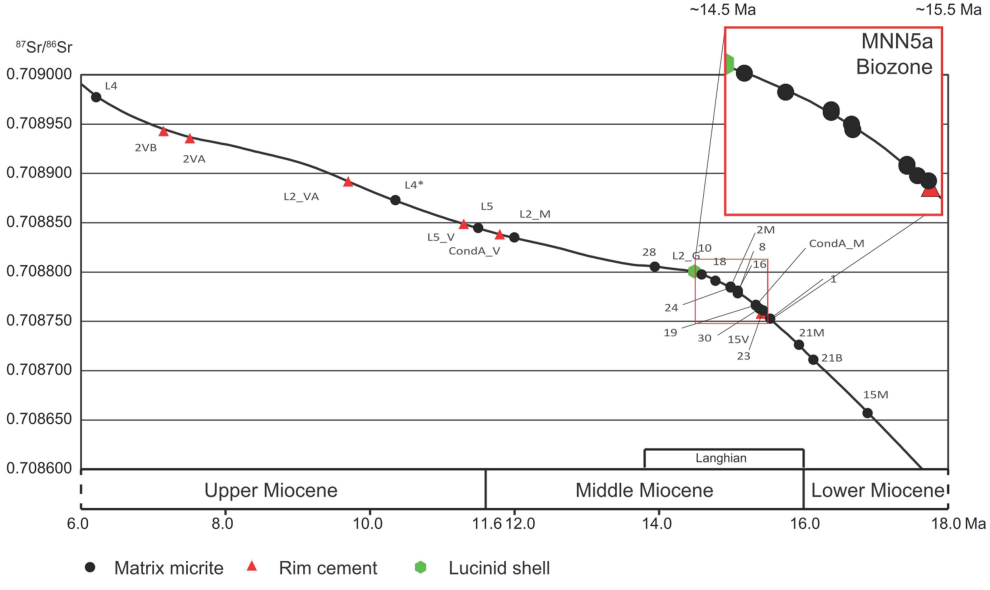
~14.5 Ma
~15.5 Ma
MNN5a
Biozone
87Sr/86Sr
0.709000
0.708950
0.708900
0.708850
0.708800
0.708750
0.708700
0.708650
0.708600
L4
2VB
2VA
L2_VA
L4*
L5
L2_M
L5_V
CondA_V
28
L2_G
10
18
2M
8
16
CondA_M
1
24
19
30
15V
23
21M
21B
15M
Langhian
Upper Miocene
Middle Miocene
Lower Miocene
6.0
8.0
10.0
11.6
12.0
14.0
16.0
18.0 Ma
Matrix micrite
Rim cement
Lucinid shell

Figure 5

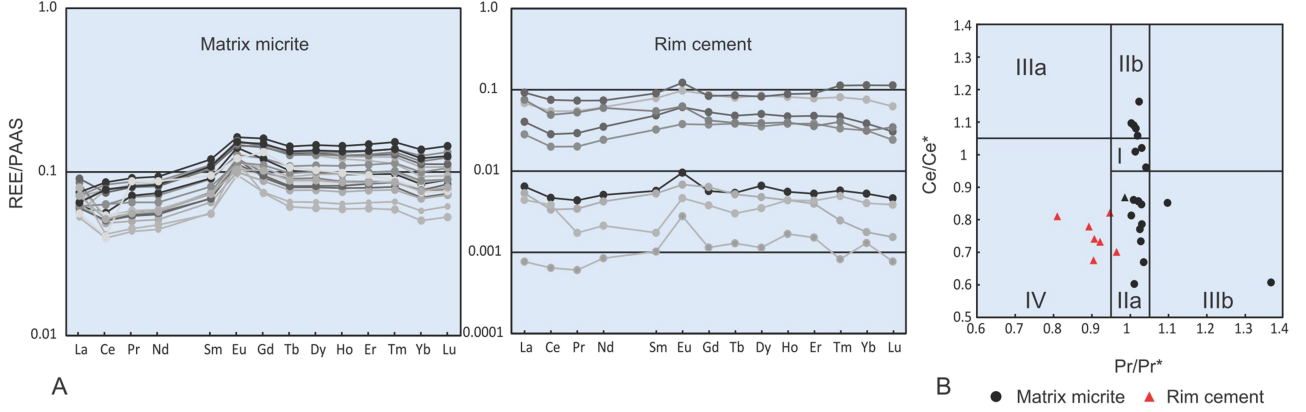
Matrix micrite
Rim cement
REE/PAAS
1.0
0.1
0.01
0.001
0.0001
La Ce Pr Nd Sm Eu Gd Tb Dy Ho Er Tm Yb Lu
A
Ce/Ce*
Pr/Pr*
IIIa
IIb
I
IV
IIa
IIIb
B
Matrix micrite
Rim cement

Figure 6

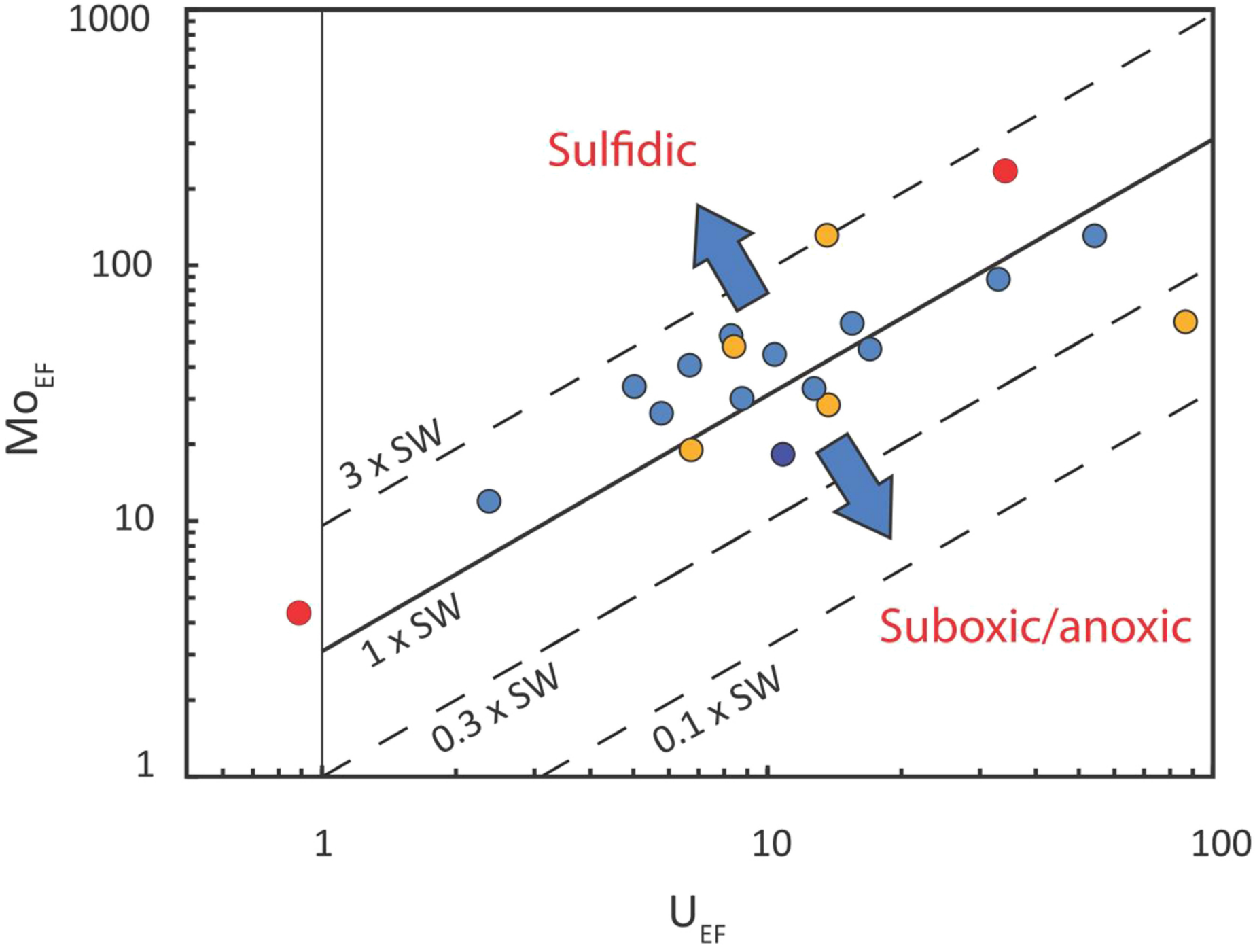
1000
100
10
1
Mo$_{EF}$
Sulfidic
3 x SW
1 x SW
0.3 x SW
0.1 x SW
Suboxic/anoxic
1
10
100
U$_{EF}$

Figure 7

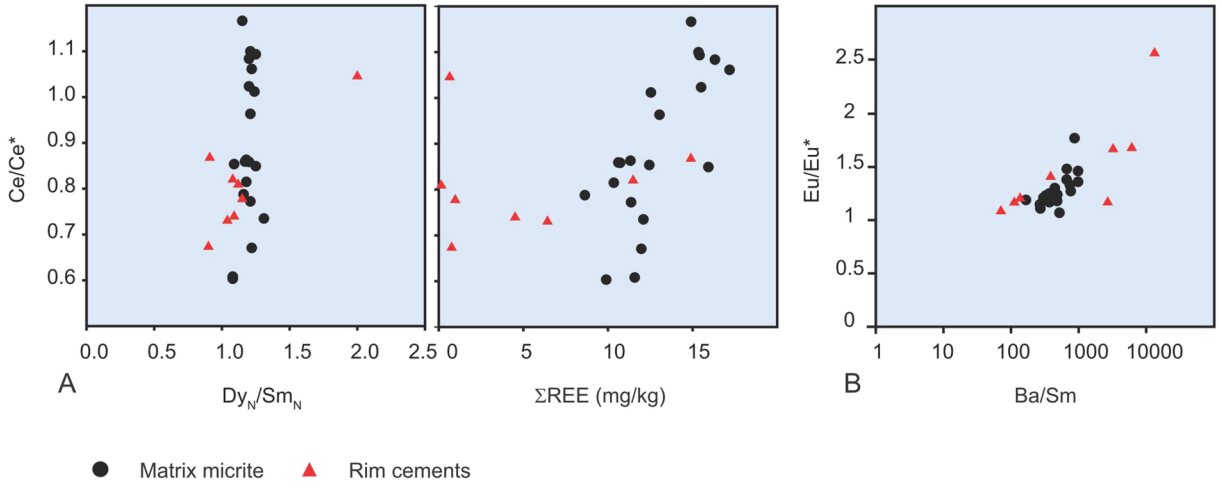
Ce/Ce*
1.1
1.0
0.9
0.8
0.7
0.6
0.0
0.5
1.0
1.5
2.0
2.5
A
Dy$_N$/Sm$_N$
0
5
10
15
ΣREE (mg/kg)
Eu/Eu*
2.5
2
1.5
1
0.5
0
1
10
100
1000
10000
B
Ba/Sm
Matrix micrite
Rim cements

Figure 8

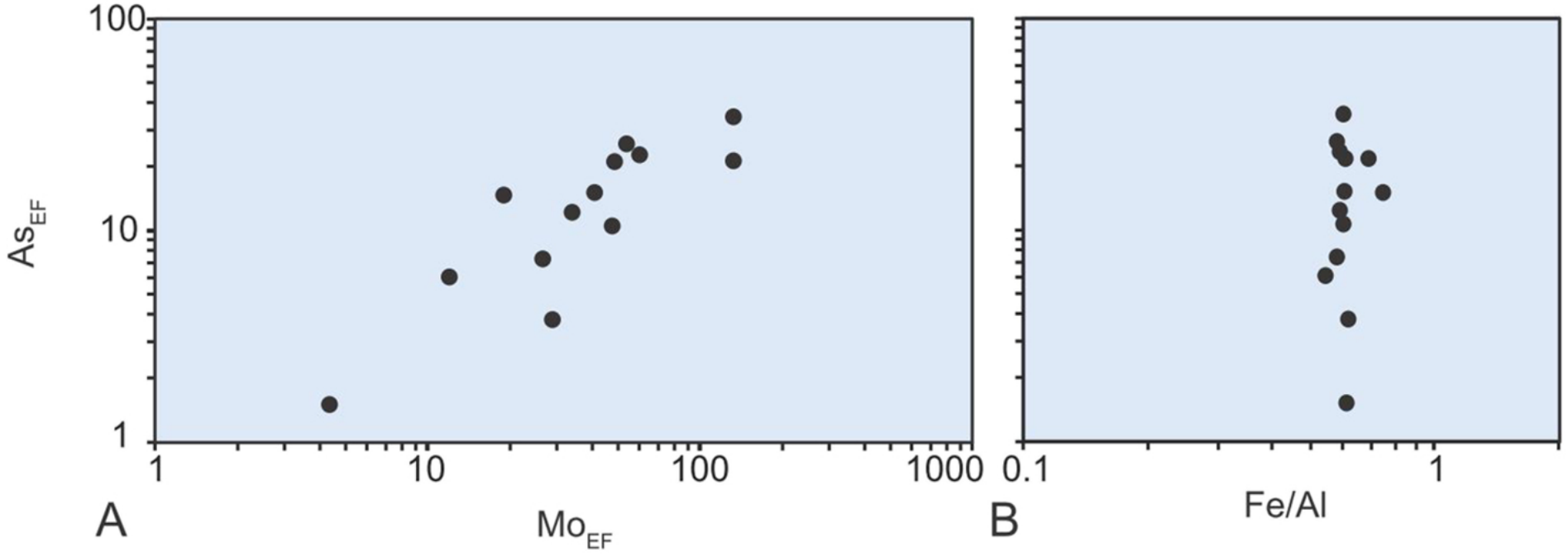

Figure 9